Contractile fibroblasts form a transient niche for the branching mammary epithelium

Jakub Sumbal [1,2,3,4], Robin P. Journot [1,3], Kriti Attri [4], Veronika Danek [4], Candice Merle [1], Marisa M. Faraldo [1], Zuzana Sumbalova Koledova [4,5] & Silvia Fre [1,3,5]

Fibroblasts are stromal cells found in connective tissue that are critical for organ development, tissue homeostasis and pathology. Single-cell transcriptomic analyses have revealed a high level of inter- and intra-organ heterogeneity of fibroblasts. However, the functional implications and lineage relations of different fibroblast subtypes remained unexplored, especially in the mammary gland. Here, we provide a comprehensive characterization of pubertal mouse mammary fibroblasts, through single-cell RNA sequencing, spatial mapping, functional assays, and in vivo lineage tracing. We unravel a transient niche-forming population of specialized contractile fibroblasts that exclusively localize around the tips of the growing mammary epithelium and are recruited from preadipocytes in the surrounding fat pad stroma. Using organoid-fibroblast co-cultures we reveal that different fibroblast populations can acquire contractile features when in direct contact with the epithelium, promoting organoid branching. The detailed in vivo characterization of these specialized cells and their lineage history provides insights into fibroblast heterogeneity and implicates their importance for creating a signalling niche during mouse mammary gland development.

Fibroblasts are cells of mesenchymal origin that form the soft connective tissue. They are endowed with extremely pleiotropic functions: they secrete, remodel, and degrade components of the extracellular matrix (ECM), produce signalling molecules to communicate with other cells, generate other types of mesenchymal/stromal cells and can become contractile and exert mechanical forces in vivo[1–3]. Through a tightly controlled spatiotemporal orchestration of all these functions, fibroblasts guide development, maintain homeostasis and support pathological changes in many organs[1]. Recent studies employing single-cell transcriptomics suggest that fibroblasts represent a heterogeneous cell population with distinct cell types or cell states specialized for different functions, presenting inter-organ conserved as well as divergent behaviour and functions[4,5]. It is not yet

understood, however, how fibroblast heterogeneity is linked to their plasticity and their origin; the question that we addressed in this study.

Epithelial ductal elongation and branching in the mammary gland occurs mostly postnatally, when a peak of oestrogen during puberty awakens the rudimentary mammary epithelium formed during embryogenesis, and the mammary epithelium actively proliferates and invades the surrounding fat pad stroma to generate a highly branched ductal network[6]. This morphogenetic function is executed by terminal end buds (TEBs), bulb-shaped and highly proliferative epithelial structures that form at the tips of the ducts and invade the surrounding stroma at the astonishing speed of 0.5 mm per day[7]. In a stochastic pattern, TEBs bifurcate to generate new branches[8,9]. The cellular and physical mechanisms that drive in vivo branching

[1]Institut Curie, Laboratory of Genetics and Developmental Biology, INSERM U934, CNRS UMR3215, PSL University, Sorbonne University, Paris, France. [2]Department of Histology and Embryology, Masaryk University, Faculty of Medicine, Brno, Czech Republic. [3]Sorbonne Université, Collège Doctoral, Paris, France. [4]Institute of Molecular Genetics of the Czech Academy of Sciences, Laboratory of Tissue Morphogenesis and Cancer, Prague, Czech Republic. [5]These authors contributed equally: Zuzana Sumbalova Koledova, Silvia Fre. ✉e-mail: zuzana.sumbalova-koledova@img.cas.cz; silvia.fre@curie.fr

morphogenesis, TEB bifurcation and ductal elongation have not been thoroughly explored.

The importance of the stroma, in particular of fibroblasts, to support mammary branching morphogenesis is well recognized[2,10]. Mammary fibroblasts secrete growth factors[11] that can induce epithelial branching[12]. Fibroblasts also secrete and remodel collagen 1[13] that supports ductal elongation in organoids[14]. Likewise, in vivo collagen deposition correlates with the direction of ductal elongation[15] and with TEB bifurcations[16]. Importantly, we have recently demonstrated that contractile mammary fibroblasts are instrumental for mammary epithelial organoid branching[17], similarly to smooth muscle cells in the budding embryonic lung[18]. We have also reported the presence of contractile α-smooth muscle actin (αSMA, encoded by *Acta2*) positive (αSMA+) fibroblasts in vivo, located around TEBs in the pubertal mammary gland undergoing branching morphogenesis[17]. Contractility is an important marker of fibroblast biology, often linked with their function and activation state during organ development[18,19], wound healing, fibrosis[20] as well as in cancer[21,22].

The transcriptional and functional heterogeneity of mammary fibroblasts during the prominent epithelial remodelling underlying pubertal branching morphogenesis in vivo has not been fully investigated. Although single cell RNA sequencing (scRNAseq) datasets of mammary fibroblasts were generated[23–28], these studies mostly analysed the mammary gland under homeostatic conditions and lacked spatial analysis and lineage tracing. Here, we have meticulously characterized the diversity of pubertal fibroblasts and identified a specialized subset of spatially restricted contractile fibroblasts that are only found at the neck of growing TEBs. We have analysed their behaviour, fate, function and origin using scRNAseq, spatial mapping, mammary transplantation assays, in vitro functional assays (including co-cultures with organoids), and in vivo lineage tracing approaches.

Results

Single cell analysis of the growing tips and the ductal regions of the pubertal mammary gland reveals the existence of contractile peri-TEB fibroblasts

The pubertal mammary gland contains fibroblasts surrounding the epithelial ducts, the TEBs and dispersed in the fat pad (Fig. 1a–c). TEBs are surrounded by a stromal niche characterized by a thickened periepithelial fibroblast layer[29] (Fig. 1b), and we recently found that peri-TEB fibroblasts express the contractility marker αSMA (Fig. 1d and Supplementary Movie 1)[17]. To study the molecular features of αSMA+ peri-TEB fibroblasts, we first performed scRNAseq on cells dissociated from micro-dissected regions of pubertal mammary glands, containing either mainly TEBs or subtending ducts. We enriched the single cell suspension for fibroblasts by a FACS negative selection (Lin^neg Ep^neg; i.e., CD45^neg, CD31^neg, CD24^neg, CD49f^neg), excluding epithelial, endothelial and immune cells[23,30,31]. After sequencing, we filtered out minor non-fibroblastic contamination and merged the TEB and duct samples to create a collective UMAP graph representing all pubertal mammary fibroblasts (Fig. 1e).

Unsupervised clustering of merged fibroblasts identified seven separate clusters (Fig. 1e). The mammary gland grows within the fat pad, so we first derived transcriptomic scores of the three major fibroblast types found in the fat pad[32]: committed preadipocytes, interstitial progenitors and adipocyte regulatory cells (AREGs), and projected the scores onto our UMAP (Fig. 1f). We observed that our clusters #2 and #3 were highly enriched in scores for interstitial progenitors and AREGs, respectively, so we annotated them as such (Fig. 1f, g). Clusters #0, #4 and #5 were enriched in the score for committed preadipocytes (Fig. 1f). Although we could detect previously discovered pro-preadipocytes[33] as clusters #0 and #4 (Supplementary Fig. 1a), we decided to merge the 3 clusters #0, #4 and #5 under the name preadipocytes for simplification of further analyses (Fig. 1g). Of interest, the two remaining clusters #1 and #6 were not

enriched in scores characteristic of fat pad fibroblasts (Fig. 1e, f) and thus likely represented mammary gland specific periepithelial fibroblasts. Comparison of the periepithelial cluster proportions between duct and TEB samples showed enrichment of cluster #1 or #6 in the different samples (Supplementary Fig. 1b) and the clusters were thus annotated as periductal (cluster #1) or peri-TEB (cluster #6) fibroblasts (Fig. 1g). We then derived a set of markers that distinguish the five resulting fibroblast clusters (Fig. 1h and Supplementary Fig. 1c) and, importantly, we found *Acta2* as a specific marker of the peri-TEB fibroblast cluster, confirming the presence of αSMA+ peri-TEB fibroblasts, as we had observed (Fig. 1d)[17].

We then used the transcriptional signatures of each cluster to inform on their relation to other fibroblasts, to identify potential functional differences between them and to position our finding with previously published studies on mammary fibroblasts. By projecting transcriptional scores of previously identified fibroblasts from adult[26] or late pubertal[27] glands, we found a remarkable conservation of most clusters. The scores of interstitial progenitors overlapped with Fib_0 or MSF-1 in previous studies, AREGs with Fib_3 and MSF4 and preadipocytes with Fib_1 and MSF-2 (Supplementary Fig. 1d, e). Periductal fibroblasts overlapped with MSF-3[27] and partially with Fib_2[26], while the signature of peri-TEB fibroblasts seems to be missing from previously published work (Supplementary Fig. 1d, e). Interestingly, the transcriptional signatures of mammary embryonic subepithelial fibroblasts[34] and breast cancer-associated myofibroblasts[23] (myCAFs) showed enrichment in the peri-TEB fibroblast cluster (Supplementary Fig. 1f, g), suggesting transcriptional conservation between fibroblasts that support highly proliferative epithelia. Moreover, we noticed that peri-TEB fibroblasts were highly enriched in contractility-related genes compared to all other clusters (Fig. 1i) and had a unique pattern of expression of ECM-associated genes, expressing less *Col1a1 and Col1a2* than AREGs, but higher levels of *Col5a1* and *Col5a2* than all other clusters (Fig. 1j). Peri-TEB fibroblasts also differed in their expression of ECM remodelling enzymes, such as matrix metalloproteinases (*Mmps*), expressing more membrane-type *Mmps* (*Mmp14, Mmp15, Mmp16*, Fig. 1j) that are important for mammary pubertal branching morphogenesis[35], and fewer soluble *Mmps* (*Mmp2, Mmp3*, Fig. 1j).

We next sought to computationally predict specific paracrine interactions and signalling networks between different fibroblast clusters and epithelial cells (both basal and luminal cells) from mammary ductal and TEB regions using the algorithm CellChat, a bioinformatic tool designed to predict significant ligand-receptor interactions between two cell types from scRNAseq data[36]. To this end, we sequenced unsorted cells from micro-dissected ducts and TEBs and selected the hormone receptor negative (HR−) and positive (HR+) luminal epithelial cells and basal epithelial cells for the analysis (Supplementary Fig. 2a–d). Interestingly, this analysis identified peri-TEB fibroblasts as the strongest signalling hub, followed by preadipocytes and periductal fibroblasts (Supplementary Fig. 3a, b). Analysis of signals emanating from fibroblasts and received by epithelial cells showed that there are little differences in the communication to either ductal or TEB epithelial cells (Supplementary Figs. 4a, b and 5a, b), corroborating the notion of their high similarity[37]. Surprisingly, this analysis revealed that FGF ligands were not expressed by peri-TEB fibroblasts but rather by fat pad-associated fibroblasts (*Fgf2* by interstitial progenitors, *Fgf7* by AREGs, and *Fgf10* by preadipocytes, Supplementary Fig. 5c). Peri-TEB fibroblasts, on the other hand, expressed higher levels of WNT ligands (*Wnt2, Wnt11*) and the WNT agonist *Rspo1* (Supplementary Fig. 5c).

A spatial atlas of mammary fibroblasts during pubertal branching morphogenesis

To define the in vivo spatial distribution of the different fibroblast clusters identified by scRNAseq, we stained histological sections and analysed the expression of genes that we found to be characteristic of

each fibroblast cluster based on the transcriptomic data (Fig. 2a and Supplementary Fig. 6a). We then annotated the regional localization of each examined field as containing predominantly ducts, TEBs or

epithelium-free fat pad (Figs. 1b and 2b). Expression of specific markers highly correlated with a defining regionalization of the different fibroblast clusters. Besides finding pan-fibroblastic markers (COL1A1,
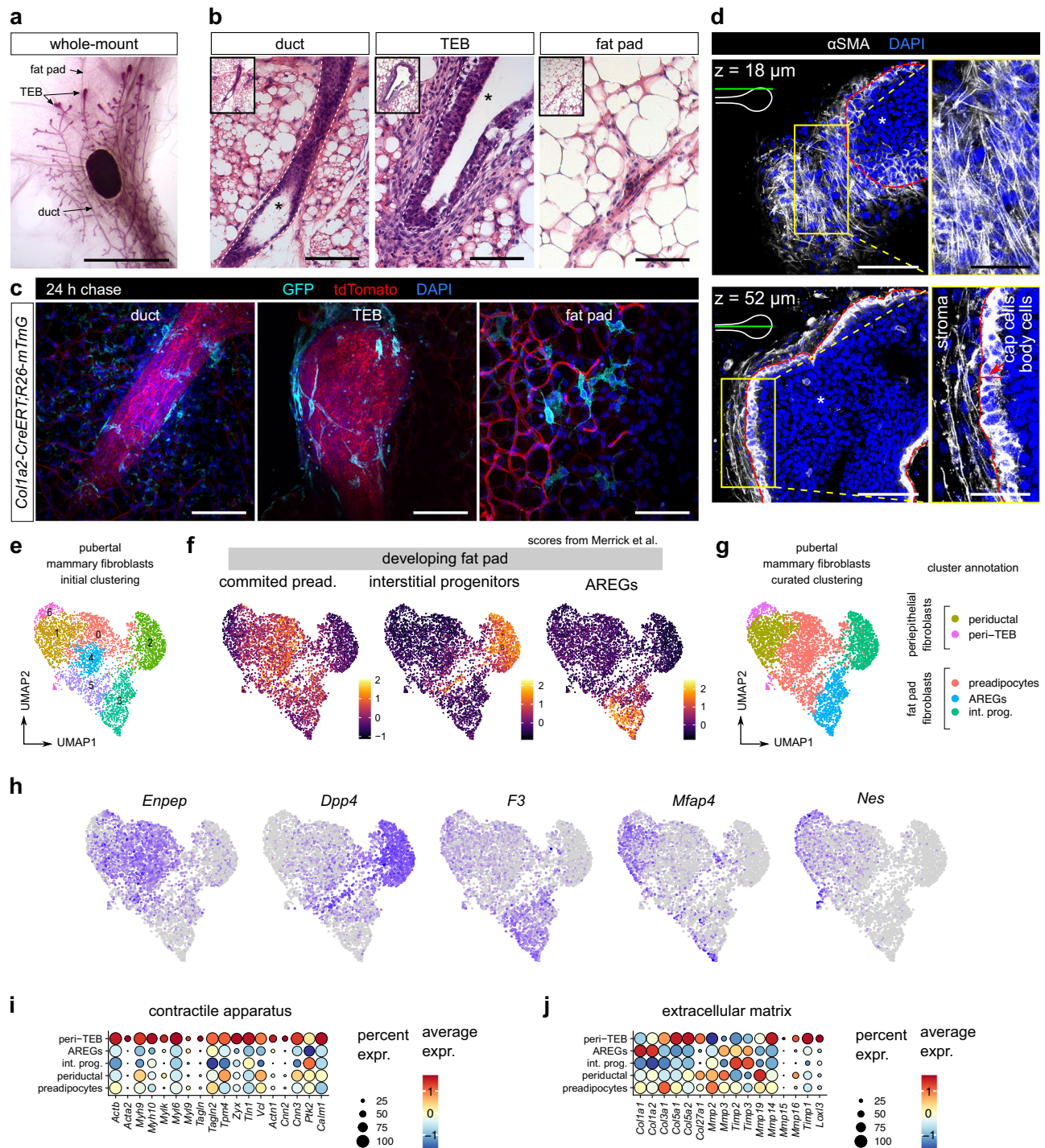
Fig. 1 | Single cell RNA sequencing of pubertal mammary fibroblasts. a A representative image of a pubertal mammary gland from a 5-week-old female mouse. Scale bar: 1 cm. **b** Histological sections of an epithelial ducts, a terminal end bud (TEB) and a fat pad region. Scale bar: 100 μm. The asterisks mark the lumen of the epithelial compartment. **c** Lineage-tracing of fibroblasts in a 5-week-old *Col1a2-CreERT;R26-mTmG* female, 24 h after tamoxifen administration. Fibroblasts are detected as GFP+ cells around ducts, TEBs and in the fat pad. Scale bar: 100 μm. **d** Immunostaining for αSMA (in white) in a cleared whole-mount mammary gland detects fibroblasts around a TEB (the TEB borders are delineated by a red line) as well as cap cells of the TEBs. The top and middle optical sections of the imaged

z-stack are presented; their localization according to the TEB is indicated by a green line. The full z-stack is presented in Supplementary Movie 1. Scale bars: 100 μm, 50 μm in detail (magnifications of the boxed areas). The asterisk marks the epithelium. **a–d** The images are representative of at least 3 biological replicates. **e** UMAP representation of sequenced mammary fibroblasts showing the different fibroblast clusters. **f** Transcriptomic scores of fibroblasts from developing fat pads[32] plotted over our dataset of mammary fibroblasts. **g** Annotation of fibroblast clusters. **h** UMAPs showing expression of cluster marker genes. **i, j** Dot plots showing the expression of contractility-related genes (**i**) and genes encoding ECM components (**j**) within the different cell clusters identified.
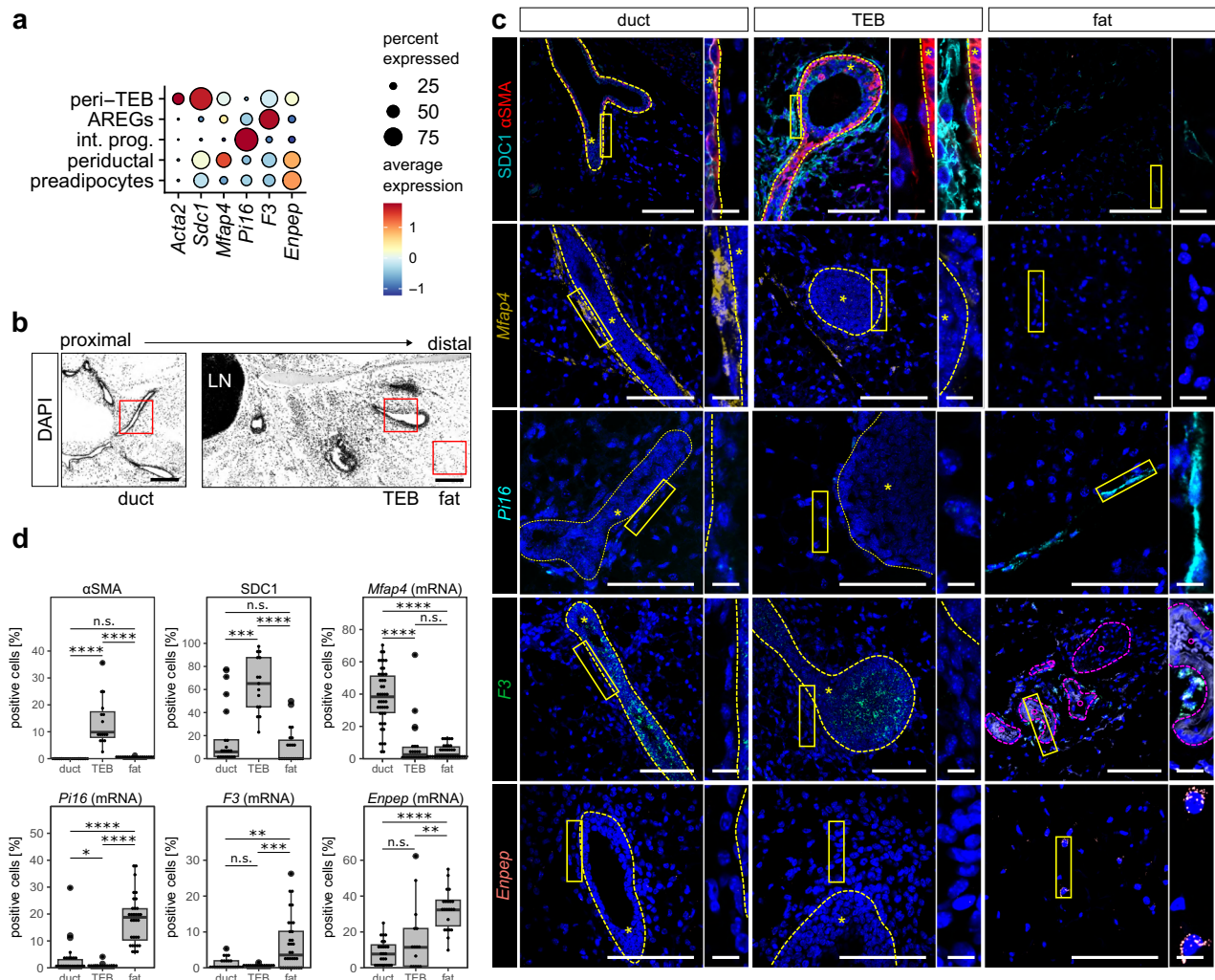
Fig. 2 | Spatial atlas of mammary fibroblasts during pubertal morphogenesis. **a** A dot plot showing expression of marker genes used for spatial mapping. **b** A representative overview of mammary gland on a histological section: red squares show fields of view (FOV) containing ducts, TEBs or distal fat pad. Scale bar: 100 μm. Representative of >5 biological replicates. **c** Representative images showing the expression of various RNA or protein markers in regions containing ducts, TEBs or distal fat pad, the insets show details on fibroblasts. * marks the epithelial compartment encircled by a yellow dashed 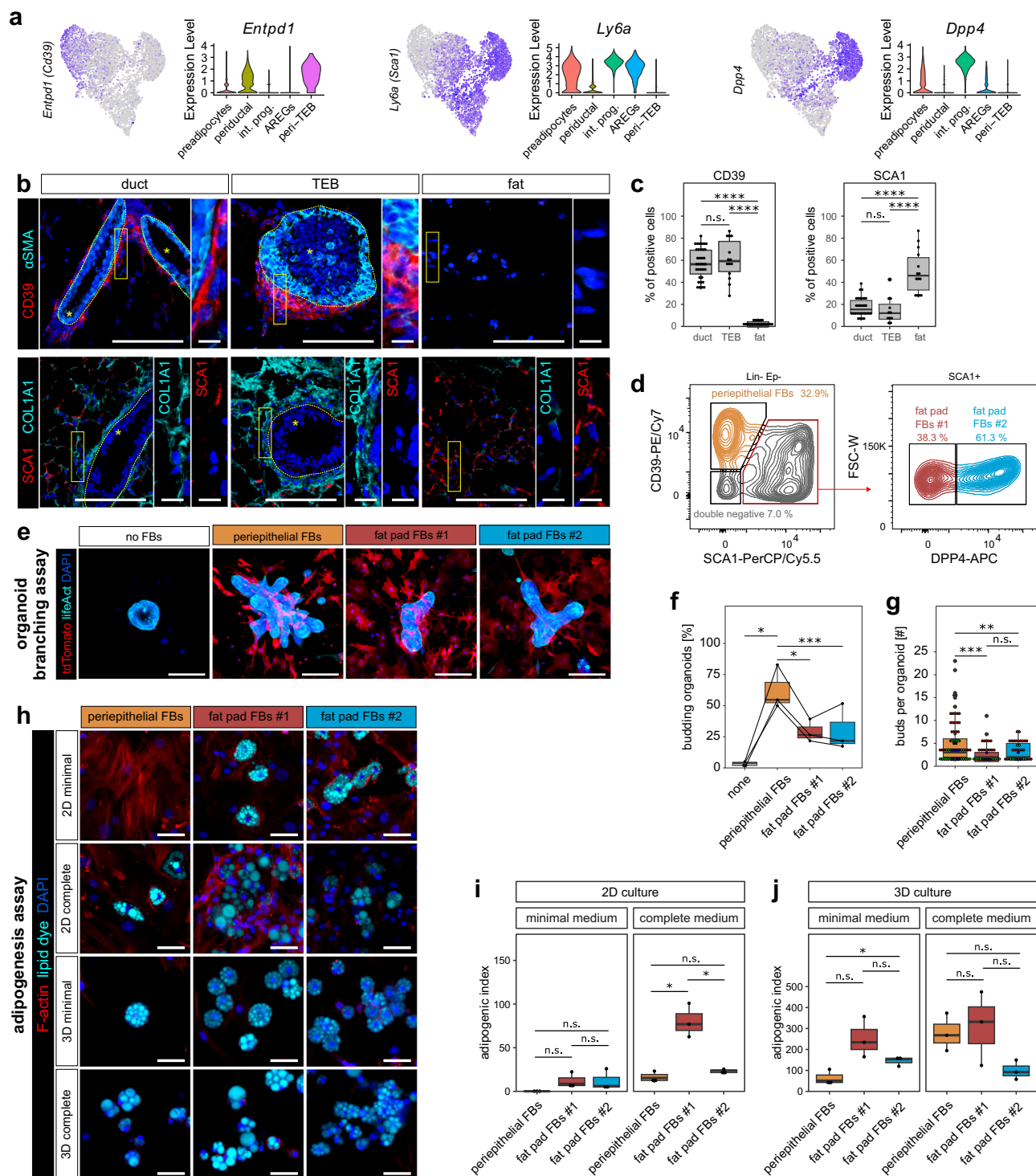line. Scale bar: 100 μm, 10 μm in detail. **d** Quantification of marker-positive stromal cells in different regions of the mammary gland, shown as box plots. Each dot represents a single FOV, $n = 3$ biological replicates, $N = 59$ FOVs for αSMA, 57 FOVs for SDC1, 113 FOVs for *Mfap4*, 90 FOVs for *Pi16*, 74 FOVs for *F3*, 81 FOVs for *Enpep*. Statistical analysis: Wilcoxon test, two-sided.

VIM) in all examined regions (Supplementary Fig. 6b, c), we could detect expression of peri-TEB fibroblast markers (αSMA, SDC1, NES, MYH10) specifically in fibroblasts around the mammary TEBs (Fig. 2c, d and Supplementary Fig. 6b, c), whereas the periductal cluster marker *Mfap4* was found in fibroblasts lining the epithelial ducts but not around TEBs (Fig. 2c, d). Furthermore, markers enriched in fat pad-associated fibroblasts (CD34 for all of them, *F3* for AREGs, DPP4 and *Pi16* for interstitial progenitors, *Enpep* for preadipocytes) were indeed located mostly in the distal fat pad (Fig. 2c, d and Supplementary Fig. 6a–c). More specifically, AREGs defined by cluster #3 were found lining blood vessels, as expected from studies in the male fat pad[38], preadipocytes were dispersed between adipocytes in the distal fat pad, and interstitial progenitors were found in the fat pad septae and in the interstitial reticulum (Supplementary Fig. 6d), a loose connective tissue at the fat pad border that creates a continuum with the septae dividing the fat pad lobules[32]. It should be noted that while the distal fat pad was analysed to represent epithelium-free adipose tissue, markers of fat pad fibroblasts were also present in the adipose tissue between ducts. To conclude, this spatial mapping demonstrates that the fibroblast clusters that we identified by scRNAseq show a high degree of spatial patterning within the mammary fat pad.

Distinct fibroblasts populations show different behaviours and functions

To assess potential functional differences between the fibroblast subsets, we sought to sort them by flow cytometry and probe them with in vitro functional assays. To this aim, we first used a negative selection (Lin[neg] Ep[neg]) to exclude immune, endothelial and mammary epithelial cells[23,30,31]. Then, we designed a FACS gating strategy based on our newly identified markers distinguishing different types of mammary fibroblasts at the RNA level (Fig. 3a) and by immunostaining (Fig. 3b, c), dividing Lin[neg] Ep^{neg} stromal cells into SCA1^{neg} CD39+ (encoded by *Entpd1*) peripithelial fibroblasts, and SCA1+ (encoded by *Ly6a*) fat pad-associated fibroblasts (Fig. 3d and Supplementary Fig. 7a, b). The latter ones were further separated into SCA1+ DPP4^{neg} fat pad fibroblasts #1, comprising preadipocytes and AREGs, and SCA1 + DPP4+ fat pad fibroblasts #2, containing interstitial progenitors (Fig. 3d). Immunofluorescence staining of freshly isolated FACS-sorted cells from pubertal mammary glands confirmed the presence of αSMA+ and NES+ peri-TEB fibroblasts specifically in the SCA1^{neg} CD39+ population (Supplementary Fig. 7c–f). Then we performed two in vitro functional tests to evaluate the capacity to promote epithelial budding/branching and the adipocyte forming potential of these different fibroblast types.

Fig. 3 | Distinct fibroblast populations show differences in morphogenetic and adipogenic capacity. a UMAP representations and violin plots showing the expression of *Entpd1* (CD39 gene), *Ly6a* (SCA1 gene) and *Dpp4* in mammary fibroblasts. **b** Representative images showing the expression of CD39 and SCA1, alongside αSMA and COL1A1, in mammary gland regions containing ducts, TEBs or distal fat pad. The insets show details on fibroblasts. The dashed yellow line demarcates the epithelial compartment, which is indicated by *. Scale bars: 100 μm, 10 μm in detail. **c** Quantification of marker positive stromal cells in different regions of the mammary gland, shown as box plots; the dots indicate single fields of view (FOV), $n = 3$ biological replicates, $N = 68$ FOVs for CD39 and 55 FOVs for SCA1. Statistical analysis: Wilcoxon test, two-sided. **d** Representative FACS plots separating mammary fibroblasts into CD39+; SCA1+ DPP4^{neg} and SCA1 + DPP4+ populations. **e**–**g** Co-culture of sorted fibroblasts with mammary epithelial organoids. **e** Representative images of organoids after 5 days of co-culture with FACS-sorted

fibroblasts (organoids in cyan, fibroblasts in red). Scale bars: 100 μm.
f Quantification of the percentage of budding organoids, shown as box plots. Each dot represents a biological replicate, lines connect paired experiments; $n = 3$ independent experiments. Statistical analysis: Student's *t*-test, two-sided.
g Quantification of the number of buds formed per organoid, where each dot represents one organoid, and the dot colours code paired experiments; $n = 3$ independent experiments, $N = 91$, 40 and 44 organoids for CD39+, DPP4^{neg} and DPP4+ population, respectively. Statistical analysis: Student's *t*-test, two-sided. **h**–**j** Adipogenesis assay on sorted fibroblasts. **h** Representative images of FACS-sorted fibroblasts after 11 days of culture in minimal or complete adipogenic medium in 2D (on plastic) or 3D (in Matrigel). Scale bars: 50 μm. **i**, **j** Quantification of adipogenic differentiation in 2D (**i**) and 3D (**j**) cultures, shown as box plots. Each dot represents a biological replicate; $n = 3$ independent experiments. Statistical analysis: Student's *t*-test, two-sided.

To assess the morphogenetic influence of the different fibroblasts on epithelial cells, we co-cultured them with primary mammary epithelial organoids in the absence of any exogenous branching-inducing growth factor. In these experimental conditions, the organoids do not bud and remain spherical, unless exposed to contractile fibroblasts[17]. We found that, while all three FACS-sorted fibroblast populations induced some degree of epithelial branching, the periepithelial fibroblasts (containing peri-TEB fibroblasts with high expression of contractility genes) presented the strongest branching-inducing capacity, both in terms of number of organoids induced to bud and in terms of number of buds/branches per organoid (Fig. 3e–g).

Next, we tested the adipogenic potential of different fibroblast types in vitro modifying a well-established method[32,38,39]. We cultured FACS-sorted fibroblasts in 2D or in 3D (Matrigel) and stimulated them with either a minimal adipogenic medium (containing only insulin) or with a complete adipogenic medium (with insulin, dexamethasone and IBMX). We observed that the fat pad fibroblasts #1 were consistently the most adipogenic population, as expected from the presence of committed preadipocytes in this cluster (Fig. 3h–j). In summary, the morphogenetic and adipogenic experiments demonstrated that all mammary fibroblast populations carry the potential to induce epithelial budding and to differentiate into adipocytes under the right conditions, highlighting their plasticity. Yet, certain fibroblast subtypes are more potent in exerting these functions, such as the periepithelial fibroblasts for bud induction (Fig. 3e–g) and the fat pad fibroblasts #1 for adipogenic differentiation (Fig. 3h–j).

Periepithelial fibroblasts mainly divide around TEBs but do not produce a long-term clonal progeny, suggesting a transient proliferative state

During pubertal growth, the mammary epithelium grows extensively to form a complex branched ductal tree that fills the fat pad[6,29]. To assess the dynamic behaviour of the different fibroblast populations identified here during such prominent organ remodelling, we evaluated their proportion by flow cytometry of mammary glands at 3 weeks of age (pre-puberty), 5 weeks (peak of puberty) and 14 weeks (adult stage). This analysis revealed the expansion of periepithelial fibroblasts relatively to other fibroblast populations (Supplementary Fig. 8a, b), consistent with the prominent increase in epithelial cells due to ductal extension and ramification. A recent study identified puberty as one of the peak times for mammary fibroblast proliferation[28]. We thus assessed if proliferative fibroblasts could act as a source for the observed periepithelial fibroblast expansion.

Our scRNAseq data indicated the presence of proliferative fibroblasts, but they did not form a separate cluster at the current resolution, but instead lied within the peri-TEB cluster, suggesting relation to peri-TEB fibroblasts (Supplementary Fig. 8c and Fig. 1e, g). A 2-h EdU pulse revealed that EdU+ cycling stromal cells were indeed mostly located near TEBs (Supplementary Fig. 8d, e), including both αSMA+ and αSMA^{neg} cells (Supplementary Fig. 8d, f). This was consistent with analysis of the proliferative cell subset from the transcriptomic data, showing heterogeneous expression of *Acta2* in proliferative cells (Supplementary Fig. 8g). Virtually all cycling cells, however, expressed the *Notch1* receptor (Supplementary Fig. 8g), that was also expressed by both periepithelial fibroblasts and preadipocytes (Supplementary Fig. 8h). We therefore used pubertal *Notch1-CreERT2;R26-mTmG* mice[40] for lineage tracing and quantified the distribution of *Notch1*-labelled fibroblasts by flow cytometry and microscopy. In this system, *Notch1*-expressing cells are labelled at the time of tamoxifen administration with permanent and heritable GFP expression. Surprisingly, *Notch1*-expressing stromal cells did not clonally expand (Supplementary Fig. 8i), but the proportion of labelled fibroblasts in different subsets changed. Clonal tracing indicated that 24 h after tamoxifen most GFP+/Notch1+ fibroblasts consisted of fat pad fibroblasts #1, showing predominant labelling of preadipocytes; however, after 1 week of chase, we detected GFP+ fibroblasts primarily within periepithelial fibroblasts (Supplementary Fig. 8j). Consistently, by whole-tissue microscopy, we found *Notch1*-expressing fibroblasts both dispersed within the fat pad and touching the epithelium at 24 h post-induction, whereas 1 week after labelling the GFP+ traced lineages either formed clusters of adipocytes in the fat pad or they were found around TEBs (Supplementary Fig. 8k).

These results indicate that, at puberty, periepithelial fibroblasts expand alongside the growing ductal epithelium and that proliferating fibroblasts are specifically concentrated around TEBs. However, lineage tracing of proliferating fibroblasts using *Notch1-CreERT2;R26-mTmG* mice showed no expansion of *Notch1*-expressing fibroblasts, suggesting that proliferating fibroblasts may represent a transient state that does not give rise to a long-term clonal progeny.

Peri-TEB fibroblasts trail behind the growing epithelium

To specifically assess the fate of peri-TEB fibroblasts we used a genetic labelling approach to lineage trace them and to follow their behaviour in vivo. *Acta2-CreERT2;R26-mTmG* mice[41] were induced at the peak of puberty to label αSMA+ peri-TEB fibroblasts (Fig. 4a, b). After 24/48 h (acute labelling) or longer chase times (1, 3, 4, 20 weeks), we quantified the proportion and distribution of GFP+ fibroblasts. Flow cytometry showed no expansion of GFP+ cells within the stromal cell population (Fig. 4c), corroborating our results from *Notch1* lineage tracing. However, while acute labelling and 1 week chase resulted in GFP+ cells only in the periepithelial population, longer chase times for 3 weeks or even 20 weeks resulted in a substantial increase in fat pad fibroblasts #1 (Fig. 4d and Supplementary Fig. 9a), suggesting that *Acta2*+ peri-TEB fibroblasts can give rise to preadipocytes in vivo.

To visualize the spatial distribution of *Acta2*+ peri-TEB fibroblasts and their progeny, we employed whole-organ imaging of CUBIC-cleared mammary glands[42,43], a method that enables evaluation of a large volume of the organ to facilitate the detection of rare cells or cells presenting an unconventional 3D shape, like fibroblasts. With a short pulse (24–48 h) of *Acta2-CreERT2* labelling, GFP+ fibroblasts were exclusively localized around TEBs, in contact with epithelial basal cells (Fig. 4e–g; note that GFP is expressed also by epithelial basal cells [Fig. 4f] and vascular mural cells [Supplementary Fig. 9b], however the level of GFP expression is considerably lower in fibroblasts than in epithelial basal cells, therefore the epithelial signal appears overexposed), whereas we could not detect any GFP+ fibroblasts surrounding the ducts (Fig. 4f, g and Supplementary Fig. 9c). Immunostaining confirmed that the GFP+ cells found in the peri-TEB stromal region 24 h after tamoxifen were indeed αSMA+ VIM+ and CD34^{neg} DPP4^{neg} peri-TEB fibroblasts (Supplementary Fig. 10a, b). After 1 or 3 weeks of chase, however, there were no more GFP+ fibroblasts around TEBs and the αSMA-labelled fibroblasts appeared to have moved to the subtending epithelial ducts (Fig. 4e–g), at a distance from the TEBs ranging from 1 to 2 mm after 1 week chase and 2.5 mm to 10 mm after 3 weeks of chase (Fig. 4h), corresponding to the distance travelled by growing TEBs in 1 or 3 weeks[7].

Peri-TEB fibroblasts differentiate into periductal fibroblasts, preadipocytes and adipocytes

Of interest, when we analysed the morphology and topology of *Acta2*-traced cells by 3D imaging after 1- or 3-week chase, we found αSMA-derived GFP+ fibroblasts either sitting on the mammary epithelial ducts or dispersed in the fat pad (Supplementary Fig. 11a, b). Based on the transcriptomic data, the combination of expression of *Entpd1* (the gene encoding CD39) and *Cd34* can divide mammary fibroblasts in 3 groups: CD39+ CD34^{neg} peri-TEB fibroblasts, CD39 + CD34+ periductal fibroblasts and CD39^{neg} CD34+ fat pad fibroblasts (including preadipocytes, AREGs and interstitial progenitors). Consistent with our previous results, we found that 3 weeks after *Acta2-CreERT2* genetic labelling, the vast majority of GFP+ fibroblasts were CD39+ CD34+
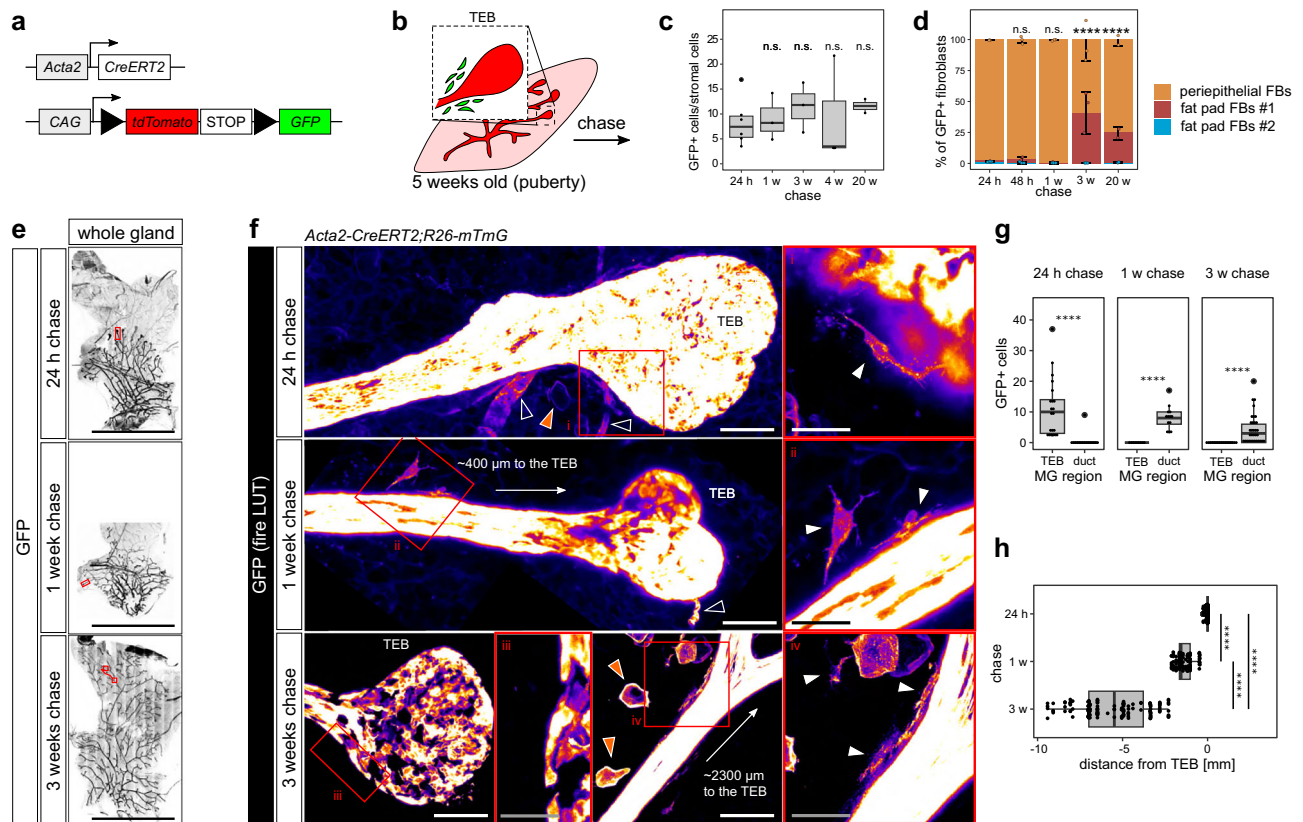
Fig. 4 | Peri-TEB fibroblasts represent a transient cell state and do not migrate with the branching epithelium. a Schematic representation of the *Acta2-CreERT2;R26-mTmG* mouse model. **b** Lineage tracing strategy for the chase experiments. **c**, **d** Flow cytometry quantification of GFP+ cells within total stromal cells (**c**) and quantification of the proportion of GFP+ fibroblasts in the 3 fibroblast populations detected by FACS (**d**); n = 3 mice per time-point. Statistical analysis: Wilcoxon, two-sided (**c**) and chi-square test (**d**). **e**, **f** Projections of z-stack imaging of whole-mount mammary glands 24 h, 1 week or 3 weeks after tamoxifen induction. Red boxes in the whole organ overviews (**e**) indicate the regions presented in (**f**) Red boxes in detailed pictures of ductal or peri-TEB regions (**f**) indicate magnified regions with GFP+ fibroblasts (in insets i–iv). The GFP channel is shown as a "fire" lookup table. White arrowheads indicate GFP+ fibroblasts, orange arrowheads indicate GFP+ adipocytes, empty arrowheads indicate GFP+ mural cells. Scale bars: 1 cm in (**e**); 100 μm in (**f**), 50 μm in insets in (**f**); the images are representative of 3 mice per time-point. **g** Quantification of the distribution of GFP+ fibroblasts in TEBs or ductal regions after 24 h, 1 week or 3 weeks of chase; n = 3 mice per time-point, N = 38 z-stack for the 24 h chase, 22 z-stacks for 1 week and 51 z-stacks for the 3 weeks chase. Statistical analysis: Wilcoxon test, two-sided. **h** Quantification of the distance of GFP+ fibroblasts from TEBs. n = 3 mice per time-point, N = 343 fibroblasts for 24 h, 106 for 1 week and 144 for 3 week-chase. Statistical analysis: Wilcoxon test, two-sided.

periductal fibroblasts, while around 10% represented CD39^{neg} CD34+ fat pad fibroblasts, and no peri-TEB fibroblast (CD39+ CD34^{neg}) was labelled by GFP (Supplementary Fig. 11c, d). Moreover, we assessed expression of the peri-TEB marker αSMA and the pan-fibroblastic marker VIM to further confirm that all αSMA+ VIM+ peri-TEB fibroblasts observed were indeed GFP^{neg} after 3 weeks of chase, while GFP+ VIM+ fibroblasts were αSMA negative (Supplementary Fig. 11e). This analysis corroborates our flow cytometry results and indicates that both periductal fibroblasts and preadipocytes can arise from αSMA+ fibroblasts, and that αSMA+ fibroblasts do not self-renew.

Further substantiating the tracing of peri-TEB fibroblasts into a (pre)adipocyte fate, after 3 weeks of chase with *Acta2-CreERT2* we found GFP+ cells with a typical adipocyte morphology and expressing perilipin 1 (PLIN1), a marker of adipocytes, which were never detected 24 h after tamoxifen, when only PLIN1^{neg} fibroblasts were labelled by GFP (Fig. 5a, b). In addition, when we isolated GFP+ fibroblasts from *Acta2-CreERT2;R26-mTmG* mice after 24 h, 3 weeks or 6 weeks of chase and tested their adipogenic potential in vitro in 3D, we did not observe efficient adipogenic differentiation after 24 h or 3 weeks of chase; however, GFP+ fibroblasts after 6 weeks of chase showed a strong adipogenic capacity (Fig. 5c, d). Of note, control GFP^{neg} cells presented comparable adipogenic capacity regardless of the time of chase (Fig. 5c).

Altogether, the lineage tracing analysis indicates that peri-TEB fibroblasts do not clonally expand during puberty and do not move forward to escort the invading epithelial TEBs, but rather lag behind the growing ducts and can either differentiate or give rise to periductal fibroblasts and later to preadipocytes and differentiated adipocytes.

Peri-TEB fibroblasts are recruited from preadipocytes
The lineage tracing experiments described above indicated that peri-TEB fibroblasts are left behind during ductal growth, raising the question of the origin of new contractile αSMA+ fibroblasts that are delivered to TEBs to maintain an equilibrium within the peri-TEB niche and to support epithelial growth and fat pad invasion. We reasoned that growing TEBs inevitably encounter preadipocytes dispersed within the fat pad on their morphogenetic journey. Moreover, we performed a trajectory analysis of our scRNAseq data and calculated a pseudo-time of differentiation, from interstitial progenitors, the putative fibroblast precursors in the fat pad[32,44], to peri-TEB fibroblasts (Supplementary Fig. 12a, b). This trajectory implies that interstitial progenitors would give rise to preadipocytes, supporting the notion that preadipocytes could act as the origin of periductal and peri-TEB fibroblasts. To experimentally test this hypothesis, we aimed to lineage trace preadipocytes to establish whether they can be recruited by growing TEBs and acquire a peri-TEB state. Our scRNAseq data
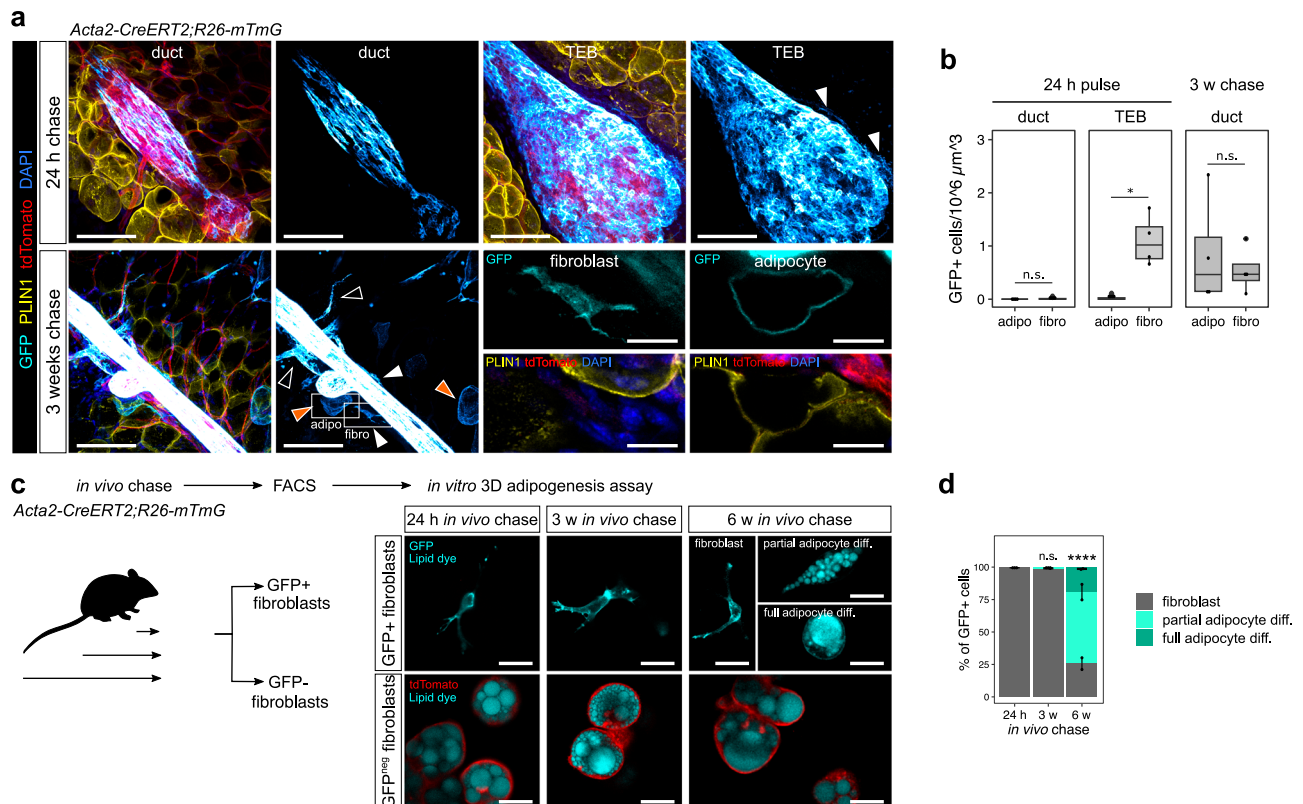
Fig. 5 | Tracing the fate of peri-TEB fibroblasts. a Projections of z-stack imaging of whole mammary glands after tamoxifen induction (24 h and 3 weeks chase). White arrowheads indicate GFP+ fibroblasts, orange arrowheads indicate GFP+ adipocytes (expressing perilipin 1, PLIN1), empty arrowheads indicate GFP+ mural cells. White boxes outline areas (fibroblasts and adipocytes) shown in detail. Scale bars: 100 μm in (**a**), 20 μm in detail. **b** Quantification of GFP+ adipocytes and fibroblasts after 24 h or 3 weeks of chase; $n = 4$ mice per time-point, $N = 38$ z-stack for the 24 h chase−duct (0.123 mm³ in total), 19 z-stacks for 24 h chase−TEB (0.127 mm³ in total), 47 z-stacks for the 3 weeks chase (0.152 mm³ in total), statistical analysis: Student's *t*-test, two-sided. **c**, **d** In vitro 3D adipogenesis assay on sorted (GFP+ and GFPneg) fibroblasts from *Acta2-CreERT2;R26-mTmG* mice after 24 h, 3 weeks or 6 weeks of chase. **c** Schematic outline of the experiment and representative images showing the morphology of sorted GFP+ and GFPneg fibroblasts after the indicated chase times. Cyan shows the lipid dye or GFP in the upper row (GFP+), while tdTomato (in red) delineates the membrane of GFPneg cells in the lower row. Scale bars: 20 μm. **d** Quantification of GFP+ fibroblast differentiation towards adipocytes; $n = 3$ independent experiments for 24 h and 3 weeks, and 2 for 6 weeks, statistical analysis: Fisher's exact test.

revealed that *Fgf10* was expressed by preadipocytes (Fig. 6a), and we confirmed its expression in preadipocytes in front of invading TEBs by in situ hybridization (Fig. 6b). We therefore used *Fgf10-CreERT2;R26-mTmG* mice[45] (Fig. 6c) to lineage trace preadipocytes at puberty and quantified the distribution of labelled fibroblasts by flow cytometry and microscopy. We observed an increase of GFP-labelled fibroblasts by flow cytometry from 24 h to 3 days; however, the number of GFP+ fibroblasts reached a plateau at 3 days of tracing and remained constant after 1 or 3 weeks (Fig. 6d). Flow cytometry analysis of the different fibroblast populations using our gating strategy revealed that the *Fgf10-CreERT2* model marked predominantly preadipocytes (represented by fat pad fibroblasts #1), but also a small percentage of periepithelial and fat pad fibroblasts #2 already 24 h after induction, and their number progressively increased with time after induction (Fig. 6e). By whole-mount imaging, we observed *Fgf10*-expressing GFP + fibroblasts (24 h after induction) in the distal fat pad and restricted to the front tip of TEBs (that we called "head"), while after 3 days or 1 week of chase, GFP+ stromal cells of fibroblast morphology were visible around the neck of TEBs, where αSMA+ peri-TEB fibroblasts reside (Fig. 6f–h). Of interest, we also found numerous GFP+ adipocytes in the fat pad that were not present at 24 h chase (Supplementary Fig. 12c, d), confirming in vivo the adipogenic potential of *Fgf10*-expressing preadipocytes. The differential localization of *Fgf10*-traced fibroblast-like cells from the invasion front of ductal extension (TEB head region) to the TEB neck and along the subtending ducts within 1 week suggested that growing TEBs recruit *Fgf10*+ preadipocytes in a very dynamic

fashion. We further confirmed the switch from preadipocytes to peri-TEB fibroblasts by immunostaining of *Fgf10-CreERT2;R26-mTmG* mice. 24 h after a tamoxifen pulse, we could not detect any αSMA+ GFP+ fibroblasts; however, their number substantially increased after 3 days and decreased after 1 week of chase (Fig. 6i, j), suggesting a peak of recruitment at 3 days, forming a transient niche for the invading TEBs. By staining with broader markers of peri-TEB fibroblasts, such as SDC1 or NES, we also saw a peak of these cells, although NES+ GFP+ and SDC1+ GFP+ cells were already present 24 h after induction (Supplementary Fig. 12e–h). These results indicate a dynamic mode of recruitment/activation of contractile fibroblasts, where the 24 h time-point catches an intermediate step of differentiation into peri-TEB cells, when preadipocytes start expressing SDC1 and NES, but not yet the contractility/fibroblast activation marker αSMA.

The recruitment of peri-TEB fibroblasts was further explored using a transplantation experiment, where we engrafted tdTomato+ fragments of mammary glands (consisting of epithelium and surrounding stroma, both labelled by red fluorescence) into cleared fat pads of immunocompromised host mice (Supplementary Fig. 13a). The tdTomato+ epithelium reconstituted a branched mammary outgrowth 3.5 weeks after transplantation (Supplementary Fig. 13b) presenting red epithelial TEBs that were surrounded by tdTomato-negative host-derived stromal cells (VIM+), while tdTomato+ engrafted stromal cells remained around proximal ducts at the original grafting site (Supplementary Fig. 13c, d). Although not in a physiological setting, this experiment demonstrates the ability of growing TEBs

to recruit host cells from the surrounding fat pad to shape the peri-TEB niche.

Furthermore, we revisited the co-culture experiment presented in Fig. 3g to analyse αSMA expression in co-cultures of mammary epithelial organoids grown with the different populations of fibroblasts sorted by flow cytometry (periepithelial fibroblasts, fat pad fibroblasts #1, and fat pad fibroblasts #2). As described above, in these co-cultures all three tested groups of fibroblasts induced epithelial budding, with the most prominent bud-inducing capacity demonstrated by periepithelial fibroblasts, although in this experimental setting organoid budding requires fibroblast contractility[17] and only peri-TEB fibroblasts (included in periepithelial fibroblasts) highly express contractility genes in vivo (Fig. 1i). We hypothesized that fat pad fibroblasts could acquire contractility when they encounter epithelial cells; therefore,

Fig. 6 | Peri-TEB fibroblasts are recruited from preadipocytes. a UMAP plot showing the expression of *Fgf10* in the different fibroblast clusters from Fig. 1e. **b** Detection of *Fgf10* expression in distal fat pad and peri-TEB areas using in situ hybridization. The dashed yellow line indicates the TEB border. The yellow boxes demarcate distal fat pad (A) and peri-TEB (B) regions shown in the magnified insets. White arrowheads point to *Fgf10*+ fat pad fibroblasts, empty arrowheads indicate *Fgf10*neg peri-TEB fibroblasts. Scale bar: 100 μm and 20 μm in insets. The image is representative of 3 biological replicates. **c** Schematic representation of the *Fgf10-CreERT2;R26-mTmG* mouse model. **d, e** Flow cytometry quantification of GFP+ cells within total stromal cells (**d**) and quantification of the proportion of GFP+ fibroblasts among the fibroblast populations defined by FACS (**e**). *n* = 4 mice per timepoint. Statistical analysis: Student's *t*-test, two-sided in (**d**) and chi-square test in (**e**). **f–j.** Immunofluorescence analysis of mammary glands from tamoxifen-induced *Fgf10-CreERT2;R26-mTmG* females after 24 h, 3 days, 1 week or 3 weeks of chase. **f** Representative images of z-stack projections of mammary gland wholemounts.

Scale bar: 100 μm. **g, h** Quantification of GFP+ fibroblasts in the TEBs and subtending duct regions (the regions are defined in schematics in **g**), as detected in wholemounts. In the box plots showing quantifications (**h**), each dot represents the number of GFP+ cells in one FOV. **f–h** *n* = 4 independent experiments, *N* = 15; 12 and 9 TEBs for 24 h, 3 days and 1 week time points, respectively. Statistical analysis: Wilcoxon test, two-sided. **i, j** Immunofluorescence analysis of mammary gland sections from tamoxifen-induced *Fgf10-CreERT2;R26-mTmG* females after 24 h, 3 days and 1 week of chase. **i** Representative images of tissue sections containing TEBs: dashed lines indicate GFP+ fibroblasts, empty arrowheads indicate GFP+ αSMAneg cells and red arrowheads indicate GFP+ αSMA+ cells. Scale bars: 10 μm. **j** Quantification of the proportion of double positive GFP+ αSMA+ cells among all GFP+ cells, shown as box plots. Each dot indicates the proportion of double positive cells in one FOV; *n* = 3 independent experiments, *N* = 12; 3 and 13 FOVs for 24 h, 3 days and 1 week of chase, respectively. Statistical analysis: Wilcoxon test, two-sided.
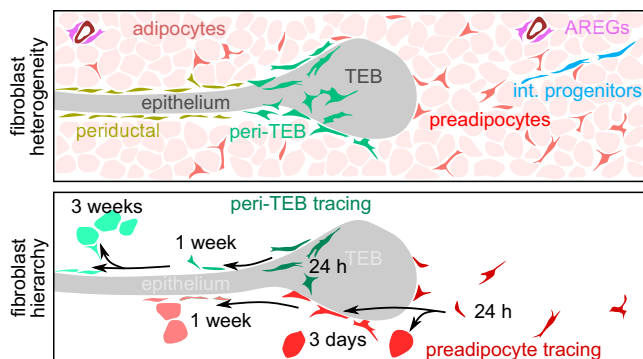
Fig. 7 | Schematic representation summarizing our findings: peri-TEB fibroblasts are recruited by the growing epithelium from preadipocytes in the fat pad. A schematic representation of our findings. Upper panel: The mammary stroma comprises 5 clusters of fibroblasts with distinct spatial locations: peri-TEB fibroblasts surround the neck of TEBs, periductal fibroblasts envelope the ducts, interstitial progenitors reside in collagenous fat pad septae, AREGs dwell in blood vessel stroma, and preadipocytes are scattered between adipocytes. Lower panel: Our lineage tracing experiments starting from peri-TEB fibroblasts (with *Acta2-CreERT2;* in green) or from preadipocytes (with *Fgf10-CreERT2;* in red) suggest that preadipocytes are recruited by the TEBs and activated into the transient peri-TEB state, then differentiate into periductal fibroblasts and later also into preadipocytes and adipocytes (black arrows).

we analysed αSMA expression in co-cultured fibroblasts. As expected, we found numerous αSMA+ periepithelial fibroblasts in co-cultures, both in fibroblasts dispersed in the Matrigel and in contact with epithelial cells (Supplementary Fig. 13e, f), which is consistent with the presence of peri-TEB fibroblasts in this population. Interestingly, fat pad fibroblasts #1 and #2, which never express αSMA in vivo, appeared αSMA+ in co-cultures only when they were touching epithelial cells (Supplementary Fig. 13e, f), suggesting that contact with the growing epithelium triggers their cell state change into "activated" αSMA+ fibroblasts. These findings demonstrate that the growing epithelium can recruit fat pad *Fgf10*-expressing preadipocytes and induce their cell state change into contractile peri-TEB phenotype.

Discussion

Heterogeneity of mammary fibroblasts

Dissection of fibroblast heterogeneity is a blooming topic of research, thanks to single cell analyses that now offer an unprecedented view into the differences between individual fibroblast subtypes presenting conserved or tissue-specific features[4,5]. In the embryonic mouse mammary gland, our recent scRNAseq analysis discriminated two distinct clusters of embryonic mammary stromal cells[34]; also, other groups identified four fibroblast clusters in the adult mammary gland[26], revealed changes in fibroblast abundance and expression of

ECM-associated genes in the aging mammary glands[25] and compared the profile of normal fibroblasts with breast cancer-associated fibroblasts[23,28]. We recently reported the existence of specialized αSMA+ peri-TEB fibroblasts that exist only in the proliferating and branching pubertal mammary gland[17]. In this study, we employed our newly discovered cluster-specific markers to draw a full picture of the spatial distribution and the fate of different fibroblasts within the mammary stroma (Fig. 7). We show that three SCA1+ clusters represent fat pad fibroblasts, previously found in the male fat pad[32,38] as well as in the adult mammary gland[26]. In this study, we focused on two periepithelial fibroblast populations, residing in the collagen-rich sheath around the mammary epithelium: periductal fibroblasts and contractile peri-TEB fibroblasts, the latter ones unique to puberty.

Our data suggest a strong correlation between spatial organization of stromal cells and different fibroblast subtypes that seems to be conserved in other organs. For example, in the skin, papillary fibroblasts are close to the epidermis, while SCA1+ reticular fibroblasts are embedded deeper in the dermis, close to the subcutaneous fat pad[46]. Likewise, in the liver, SCA1+ peri-portal fibroblasts sit in the portal area and form a separate scRNAseq cluster, distinguished from hepatic stellate cells that line hepatocytes[47,48]. We thus propose that the spatial patterning of fibroblast subtypes may reflect the niche-specific needs for ECM, as ECM-related genes represent the major discriminators of fibroblast subtypes across different organs[5].

Fibroblast hierarchy

Fibroblasts are stromal cells of remarkable plasticity, as revealed by genetic lineage tracing experiments and transplantation assays. In the skin, papillary and reticular fibroblast lineages segregate during embryonic development and never overlap in adult homeostasis[46]. In the inguinal fat pad, *Dpp4*+ interstitial progenitors can contribute to both preadipocytes and AREGs in a unidirectional way[32,44], in agreement with transcriptomic analyses that identified *Pi16*+ *Dpp4*+ fibroblasts as a progenitor population sitting at the top of the fibroblast hierarchy[4]. Our lineage tracing experiments show that the newly discovered peri-TEB fibroblasts can contribute to both periductal fibroblasts and preadipocytes, but in agreement with aforementioned studies, we never observed them to give rise to *Pi16*+ *Dpp4*+ interstitial progenitors. Importantly, we also identified preadipocytes as an in vivo source population for activated peri-TEB fibroblasts.

Based on our lineage tracing experiments with three different mouse lines, we propose that proliferative fibroblasts represent cells transiting between a preadipocyte (*Fgf10*+) and a peri-TEB (*Acta2*+) state. Furthermore, lineage tracing experiments with *Notch1-CreERT2* mice, targeting most proliferative fibroblasts, did not show any clonal expansion of the traced cells, conflicting with the possibility that proliferative TEB fibroblasts could act as the source for the other classes of fibroblasts. We cannot, however, formally disprove the possibility that a rare population of *Acta2* negative/*Notch1* negative

proliferative fibroblasts that was not represented in the scRNAseq dataset, may exist around TEBs and remain associated with the TEBs as they grow, and that it may generate peri-TEB fibroblast daughter cells on the way. Similarly, the 2-h EdU pulse used to detect proliferative fibroblasts may have missed slowly proliferative cells that would escape our analysis.

We show by ex vivo recombination that both preadipocytes and interstitial progenitors can be activated by contact with the epithelium and acquire a contractile αSMA+ phenotype, although it is not clear whether interstitial progenitors can change directly into peri-TEB fibroblasts in vivo, or if they must transition through a preadipocyte state. Similarly, without further lineage tracing studies, we cannot formally rule out the possibility of other stromal cell types, like pericytes or adipocytes, acting as a source for the peri-TEB fibroblasts, either directly or through other fibroblast subtypes. Thus, our results support the notion that peri-TEB fibroblasts represent a transient cell state forming a specialized niche during branching morphogenesis and provide the missing link between fat pad fibroblasts and periepithelial fibroblasts, demonstrating that they are not separate lineages (Fig. 7).

Fibroblasts can also differentiate into pericytes and adipocytes in the skin[49,50] and in the interscapular, inguinal[51], mesenteric and gonadal fat pad[44]. In the mammary gland, adipocytes de-differentiate into fibroblasts during pregnancy and are re-established from fibroblasts during involution[52,53]. Our in vitro experiments demonstrate that both periepithelial and fat pad fibroblasts harbour adipogenic potential. By lineage tracing in vivo, we demonstrate that preadipocytes can swiftly differentiate into adipocytes during pubertal development. Interestingly, we show in vivo that also peri-TEB fibroblasts can produce adipocyte progenies, although after longer time. Our findings suggest that peri-TEB fibroblasts have little adipogenic potential and may need longer time to differentiate into periductal fibroblasts and/or preadipocytes to produce mature adipocytes. It is yet to be determined which mammary fibroblast clusters can differentiate into adipocytes in adult homeostasis and during pregnancy-associated changes of the mammary stroma. Our data showing the remarkable plasticity of these cells indicate that both fat pad and periepithelial fibroblasts can give rise to adipocytes in vivo.

Fibroblasts orchestrate epithelial morphogenesis

Fibroblasts are believed to be critical regulators of mammary branching morphogenesis[2,10], thanks to their capacity to secrete fibroblast growth factors (FGFs)[11]. FGF10 acts as a chemoattractant in organoids[11] and FGF10-soaked beads locally accelerate branching when implanted in vivo[8]. *Fgf10* was shown to be specifically expressed by the preadipocyte cluster (called Dpp4⁻−1 or MSF-2) by scRNAseq[26,27] and these cells were reported to be more abundant close to TEBs rather than ducts[27]. Our detailed histological analysis shows, however, that *Fgf10*-expressing preadipocytes are mostly dispersed in the fat pad. While most epithelial cells are shielded from the fat pad by a dense collagenous stroma, the leading edge of TEBs (TEB "head") is in direct contact with *Fgf10*-expressing preadipocytes. This could explain why preadipocytes were found in the peri-TEB stroma[27], but it is important to note that the activated αSMA+ peri-TEB fibroblasts that wrap around the TEB neck do not express *Fgf10*. Thus, the spatial organization of fibroblast clusters could explain how FGF10-mediated chemoattraction acts in vivo.

FGF2 induces epithelial proliferation and organoid budding in vitro[12], which is reminiscent of mammary side branching[54]. Here, we found that FGF2 is produced by interstitial progenitors, located along the septae dividing the fat pad. These stromal cells could stochastically encounter a growing duct; however, whether this impacts the pattern of epithelial branching is an attractive hypothesis that remains to be mechanistically explored. We have also detected cluster-specific Wnt ligand expression, and peri-TEB fibroblasts represent the strongest producers of Wnt ligands, suggesting that they may create a Wnt ligand-rich growth-promoting niche around TEBs. Other paracrine signals predicted to act between fibroblasts and epithelial cells by CellChat analysis, which we provide here, remain to be functionally investigated.

ECM expression and organization is another critical regulator of mammary epithelial branching[55–57] and our scRNAseq analysis reveals distinct patterns of ECM-associated gene expression in different fibroblast clusters. Specifically, our analysis shows that peri-TEB fibroblasts express low levels of collagen 1, but higher levels of collagen 5, suggesting that there may be a composition shift in the collagen sheath after their transition into periductal fibroblasts. It remains to be studied, however, how the change of biochemical composition impacts on the physical properties of the matrix. Peri-TEB fibroblasts are also the primary source of membrane bound MMPs that can further promote basal membrane thinning and were shown to facilitate mammary branching in vivo[35].

A new line of evidence suggests that stromal cells may also regulate epithelial morphogenesis through mechanical forces derived from actomyosin cell contraction, as it was shown for the regulation of lung branching[18,58], the growth of feathers[59] and hair follicles[60] as well as gut villification[61]. In the mammary gland, we recently demonstrated that fibroblast contractility drives epithelial organoid branching in a co-culture system[17]. Although functional evidence of peri-TEB contractility in vivo is still missing, it is conceivable that the fibroblasts positioned around the neck of TEBs that we studied here may create a hoop stress that facilitates the ductal invasion through the fat pad, as previously suggested for myoepithelial cells[62]. Of note, the peculiar localization of peri-TEB fibroblasts correlates with the transition of the cuboidal epithelial cap cells of TEBs into spindle-shape myoepithelial/basal cells lining the subtending ducts, opening the exciting opportunity to test the involvement of contractile fibroblasts in this process. In conclusion, we have characterized a fibroblast population that creates a specialized mechano-chemical niche to facilitate epithelial morphogenesis (Fig. 7). It should be noted that other stromal cells, including adipocytes, as well as macrophages, lymphocytes, dendritic cells, endothelial cells, pericytes, nerve cells and others are also important sources of signaling molecules that could have instructive roles for epithelial growth. Furthermore, duct versus TEB differences in epithelial cells may also account for changes in the basement membrane structure or composition. However, this study specifically focused on the characterization of fibroblasts in the pubertal mammary gland.

Fibroblasts activation—signals from the epithelium and beyond

The process of fibroblast activation is best studied in wound healing, when fibroblast contractility and ECM production are turned on to aid proper wound closure and healing. Excessive fibroblast activation, however, can result in scarring, fibrosis and provide a cancer-prone microenvironment. Contractile fibroblasts are also found in developing tissues and it is not clear if they are controlled by conserved mechanisms. Interestingly, we found that, while peri-TEB fibroblasts are characterized by a signature of contractility, they express lower levels of collagen 1, suggesting that the activation process is either completely different or only partial, when compared to wound healing. Many of the signalling pathways commonly associated with fibroblast activation were shown to be involved in mammary fibroblasts regulation, like PDGF[63], FGF[64] or WNT signalling[65–67]. Contact with macrophages can activate myofibroblasts in wounds, via cell-cell adhesion and TGFβ signalling[68]. Macrophages are present in the peri-TEB stroma and their depletion impairs mammary outgrowth[69,70]. It is therefore tempting to speculate that TEBs invading the fat pad create a miniature wound-like environment, involving activation of contractile fibroblasts that are recruited to propel epithelial branching in an evolutionary conserved manner. Further research into fibroblast activation during

organ development is needed to understand the differences and similarities between morphogenesis, wound healing, fibrosis and cancer.

Methods

Ethics statement

All procedures involving animals were performed under the approval of the Ministry of Education, Youth and Sports of the Czech Republic (license # MSMT-9232/2020-2), supervised by the Expert Committee for Laboratory Animal Welfare of the Faculty of Medicine, Masaryk University, at the Laboratory Animal Breeding and Experimental Facility of the Faculty of Medicine, Masaryk University (facility license #58013/2017-MZE-17214), or under approval of the Animal Facility Committee of the Institute of Molecular Genetics of the Czech Academy of Sciences and the Czech Academy of Sciences (licence #AVCR 1066/2024 SOV II) at the Animal Facility Module of the Czech Centre for Phenogenomics (facility license #MZE-59270/2024-13143), or under the approval of the ethics committee of the Institut Curie and the French Ministry of Research (reference #34364-202112151422480) in the Animal Facility of Institut Curie (facility license #C75-05-18).

Mice

ICR mice and nude mice were obtained from the Laboratory Animal Breeding and Experimental Facility of the Faculty of Medicine, Masaryk University. *LifeAct-GFP* mice were created by Wedlich–Söldner team[71], *R26-mTmG*[72], *Col1a2-CreERT*[73] and *Acta2-CreERT2* mice[41] were acquired from the Jackson Laboratory. *Notch1-CreERT2* mice[40] were created in our laboratory. *Fgf10-CreERT2*[45] mice were a kind gift from Saverio Bellusci. Transgenic animals were maintained on a C57BL/6 background. Experimental animals were obtained by breeding of the parental strains, the genotypes were determined by genotyping. The mice were housed in individually ventilated or open cages, all with ambient temperature of 22 °C, a 12 h:12 h light:dark cycle, and food and water ad libitum. Only female mice were used for this study, as pubertal mammary gland development is a sex-specific developmental trait. For induction of *CreERT2* constructs, 5-week-old pubertal female mice were treated with a single dose of tamoxifen (Sigma, 2 mg/10 × g of mouse) diluted in corn oil (Sigma), delivered via intraperitoneal injection. For EdU incorporation assay, 5-week-old wild-type females were injected with EdU 10 nmol/1 × g of mouse, delivered via intraperitoneal injection 2 h prior to euthanasia. Mice were euthanized by cervical dislocation and mammary gland tissues were collected immediately.

Microdissection of TEB/duct

For microdissection of TEB- and duct-containing regions, 5 weeks old *R26-mTmG* homozygoes females were used. Mammary glands #3 and #4 were dissected and spread on 10 cm plastic petri dishes. Under the control of a fluorescent stereoscope (Leica FM165C), 0.5 × 0.5 mm pieces of tissue containing either TEBs or pieces of ducts (assessed based on tdTomato fluorescence) were dissected and collected in CO_2 independent medium on ice. 8–11 mice were pooled for one experiment.

Single cell RNA sequencing

For scRNAseq experiments, microdissected pieces of mammary gland were digested in a collagenase/hyaluronidase solution [3 mg/ml collagenase A, 100 U/ml hyaluronidase (all Merck), 5% fetal bovine serum (FBS; Hyclone/GE Healthcare) in CO_2 independent medium (Thermo Fisher Scientific)] for 2 h at 37 °C, shaking at 120 rpm. Resulting tissue fragments were treated with 0.25% trypsin, 5 mg/ml dispase II, 100 μg/ml DNase and red blood cell lysis buffer (Sigma) and filtered through a 40 μm cell strainer. Resulting single cell suspension was spun down and resuspended in staining medium (10% FBS, 100 U/ml penicillin, and 100 μg/ml streptomycin in CO_2 independent medium) with

antibodies for negative selection (Supplementary Table 2) and incubated on ice in dark for 30 min or directly resuspended in flow buffer (5 mM EDTA, 1% BSA, 1% FBS in phenol red-free DMEM/F12 with HEPES) for single cell RNA sequencing of unsorted cells. Then, the cells were washed twice with PBS, resuspended in flow buffer and filtered through a 40 μm cell strainer. The analysis was done on or Fusion (BD), operated by SORP software (BD). The resulting cell pellet was pooled down, resuspended in freezing medium (10% DMSO in FBS) and frozen by slow freezing at −80 °C and moved to liquid nitrogen 24 h thereafter. Single-cell suspensions were prepared and processed using the GEM-X Single Cell 3′ kit (10× Genomics) following the manufacturer's protocol for frozen cells, targeting 10,000 cell per sample with sequencing depth of 100,000 reads per cell. Raw sequencing reads were processed using Cellranger (v7.1.0). The Cellranger summary report estimated the following cell numbers, 5048 cells for ductal sample (stroma), 457 cells for TEB sample (stroma), 7716 cells for duct (unsorted) and 6066 cells from TEB (unsorted), with the respective mean reads per cell 173,715; 830,616; 66,682 and 64,340.

scRNAseq data analysis−data preprocessing

The analysis of scRNAseq data was performed in R (R systems) using the Seurat (v5.3.0) package[74]. The following filters were applied to the data to remove doublets and damaged cells: genes with expression in <3, *nCount_RNA* < 10000 or > 80000, *nFeature_RNA* < 3500 or with a percentage of mitochondrial reads > 5 were removed. The data were normalized with the *SCTransform* function. Uniform Manifold Approximation and Projection and neighbors identification were computed using the *RunUMAP* and *FindNeighbors* function on the first 10 PCs Clusters were defined using the *FindClusters* function with a resolution set to 0.2–0.7, depending on the sample. Fibroblast, epithelial and leukocyte populations were then identified based on canonical markers (*Col1a1*, *Col3a1*, *Pdgfra* for fibroblasts; *Ptprc* for leukocytes; *Epcam*, *Cdh1* for epithelium).

scRNAseq data analysis−subpopulation analysis

The fibroblasts were then merged together and reanalysed using the first 12 PCs for *RunUMAP* and 0.3 resolution for *FindClusters*. Pericyte contamination was identified by *Des* expression and excluded from the analysis. Cluster markers were calculated using the *FindAllMarkers* function. The expression scores were calculated using the *AddModuleScore* function with genes in Supplementary Table 1.

scRNAseq data analysis−cell communication analysis

Communication link between cell populations were identified using the CellChat (v1.5.0) R package[36]. Only epithelial and fibroblast clusters were used for this analysis. Interactions between the different clusters were identified based on the mouse "Secreted Signaling" internal CellChat database. Interactions identified in less than 5 cells per group were filtered out. Interactions between groups were visualized using the "netVisual_chord_gene" function.

Cell transition trajectory and pseudo-time analysis

We used the R package destiny (v3.12.0) and SingleCellExperiment (v1.20.1) to calculate the transition probabilities between cells and build the diffusion map. We then plot the trajectory according to the two first diffusion components. We then used slingshot (v2.6.0) to define pseudotime, specifying the cluster "Interstitial progenitor"s as source and the cluster "peri-TEB" as end point.

Immunohistochemistry (IHC)

For IHC, only mammary glands #4 were dissected, spread on a glass slide and fixed in 4% paraformaldehyde (EM grade; Electron Microscopy Sciences) overnight at 4 °C, then they were dehydrated in ethanol solutions with increasing concentration and in xylene and embedded in paraffin. 5 μm sections were cut on rotational microtome

(Thermo Scientific, Microm HM340E or Leica RM2255). After rehydration, sections were boiled in pH 6 citrate buffer or pH 9 Tris-EDTA buffer to retrieve antigens, blocked in 1% BSA and 5% FBS and incubated with primary antibodies (Supplementary Table 2), fluorophore-conjugated secondary antibodies (Thermo Fisher Scientific) and 1 μg/ml 4',6-diamidino-2-phenylindole (DAPI, Merck), mounted (Aqua Poly/Mount, Polysciences or Fluromount, F4680, Sigma) and imaged on laser scanning confocal microscope LSM780/800/880/900 (Zeiss). The IHC-IF of *Fgf10* mouse model were imaged on spinning disk confocal microscope (Nikon CSU-W1). For SCA1 staining, slides were first stained for COL1A1, then with biotin-conjugated SCA1 primary antibody, followed by incubation with 1 μg/ml AlexaFluor633-conjugated streptavidin (Thermo Fisher Scientific) for 1 h before counterstaining with DAPI. EdU detection was performed using Click-iT imaging kit (Thermo Fisher Scientific) following the manufacturer's instructions. The quantification of positive cells was done manually in ImageJ, using DAPI signal to count total stromal cell number. Cells of epithelial ducts and blood vessels, recognized by typical morphology, autofluorescence and cell shape, were omitted from analysis. The field of views (FOVs) were all of the same size (212 × 212 μm) and were scored "duct", "TEB" or "fat" based on morphology and position of the structures (TEBs: stratified epithelium, bulb-like shape and position of the structure at the distal part of the mammary epithelium (invasive front); duct: bi-layered epithelium; fat: no epithelial structures in the FOV).

In situ hybridization (ISH)

For ISH, mammary glands were processed the same way as for IHC and the staining was performed using the RNAScope kit following manufacturer's instructions, using commercially available probes (Supplementary Table 2). The quantification of positive cells was done manually in ImageJ, similarly to IHC quantification, using the DAPI signal to count the total stromal cell number. Rules for determining positive cells were unique for each probe, based on the level of expression (3 dots for *Enpep* and *Ly6a*; cytoplasm full of dots for *F3*, *Pi16*, *Mfap4* and *Fgf10*).

Fluorescence assisted cell sorting (FACS)

For FACS or flow cytometry, harvested mammary glands #1, #2, #3, #4 and #5 were chopped into 0.5 × 0.5 × 0.5 mm³ pieces and digested in a solution of collagenase and trypsin [2 mg/ml collagenase A, 2 mg/ml trypsin, 5 μg/ml insulin, 50 μg/ml gentamicin (all Merck), 5% FBS (Hyclone/GE Healthcare) in DMEM/F12 (Thermo Fisher Scientific)] for 30–60 min at 37 °C. Resulting tissue suspension was treated with DNase I (20 U/ml; Merck) and red blood cell lysis buffer and filtered through 40 μm cell strainer to achieve single cell solution. The cells were resuspended in staining medium with antibodies (Supplementary Table 2) and incubated on ice in dark for 30 min. Then, the cells were washed twice with PBS, resuspended in flow buffer and filtered through a 40 μm cell strainer. The analysis was done on Aria III or Fusion (both BD), operated by SORP software (BD). The flow cytometry data were analysed using the FlowJo software (BD).

In vitro adipogenesis assay

For in vitro assessment of adipogenic potential in 2D, 20,000 FACS-sorted fibroblasts were seeded in one well of an IBIDI 8-well plate. For the 3D conditions, 30.000 FACS-sorted fibroblasts were mixed with 30 μl of Matrigel, plated in one well of an IBIDI 8-well plate and left to solidify for 30 min before media addition. The cells were overlayed with minimal adipogenic medium (MAM; 10% FBS, 1× ITS (10 μg/ml insulin, 5.5 μg/ml transferrin, 6.7 ng/ml sodium selenite), 100 U/ml of penicillin, and 100 μg/ml of streptomycin in DMEM/F12) and incubated overnight. The next day, the medium was replaced by either fresh MAM or by a complete adipogenic medium [CAM; 1 μM dexamethasone, 0.5 μM 3-isobutyl-1-methylxanthin (IBMX) in MAM]. After

2 days of CAM (or MAM) treatment, the medium was switched back to MAM for all conditions and cells were kept in culture for 8 more days with medium replaced every other day. Then the cells were fixed with 4% PFA for 30 min, permeabilized with 0.5% Triton -100 in PBS for 10 min and stained with DAPI (1 μg/ml), AlexaFluor 568 phalloidin and BioTracker 488 Green Lipid Droplet Dye (Sigma) overnight. Cells were rinsed with PBS and imaged on a confocal microscope LSM 880 (Zeiss).

For quantification of the in vitro adipogenesis, adipogenesis index was calculated as shown before[32], using the ImageJ. To calculate the number of nuclei, the channels were split, Gaussian Blur applied, thresholding and binarization of the image was and counted the number of nuclei with the "analyze particles" function. For the lipid dye channel, Gaussian blur was applied, thresholding performed, and the area of above-the-threshold signal was calculated. The adipogenesis index was calculated as area of lipid dye signal above threshold divided by number of nuclei. The threshold value was always kept the same for all wells of a given experiment.

In vitro adipogenesis assay of lineage traced cells

For adipogenesis assay with in vivo lineage traced cells, The *Acta2-CreERT2;R26-mTmG* mice were induced at 5 weeks of age and processed for FACS sorting after 24 h, 3 weeks or 6 weeks. 2–4 mice were pooled for one preparation and counted as one experimental replicate. The fibroblast isolation and FACS were performed as described above, using the negative selection (CD45neg CD31neg CD24neg CD49fneg) to enrich for fibroblasts by FACS. 12,000 GFP+ fibroblasts (or all GFP+ fibroblasts available) and 12,000 GFPneg control fibroblasts were seeded in 15 μl Matrigel dome, overlayed with MAM after 30 min of solidification; the next day, the medium was changed to CAM for 2 days and cells were kept for 8 more days in MAM, changing the medium every 2 days. At the end of the experiment, cells were fixed and processed for staining as described above. The adipogenesis was quantified by manually staging the GFP+ cells as either fibroblastic (spindle shaped, no lipid droplets), partial adipocyte differentiation (small lipid droplets, non-round shape) or full adipocyte differentiation (round shape, big lipid droplets). All GFPneg fibroblasts efficiently underwent adipocyte differentiation.

Immunocytochemistry (ICC)

For immunofluorescent analysis, 10,000 FACS-sorted fibroblasts were plated directly on coverslip-bottom 8-well plates (IBIDI) and cultured for 12 h in fibroblast medium [10% FBS, 1× ITS (10 μg/ml insulin, 5.5 μg/ml transferrin, 6.7 ng/ml sodium selenite), 100 U/ml of penicillin, and 100 μg/ml of streptomycin in DMEM], fixed with 4% formaldehyde for 15 min, permeabilized with 0.5% Triton X-100 in PBS for 10 min and blocked with PBS with 10% FBS for 30 min. Then the cells were incubated with primary antibodies (Supplementary Table 2) for 2 h at RT. After washing, the cells were incubated with fluorophore-conjugated secondary antibodies (Thermo Fisher Scientific) and phalloidin AlexaFluor 488 and DAPI (1 μg/ml) for 2 h at RT. The cells were imaged using LSM780/880/900 (Zeiss).

Whole mount clearing and imaging

Staining and clearing of the mammary glands was done following clear, unobstructed brain imaging cocktails (CUBIC) protocol[42,43]. Briefly, mammary glands #3 or #4 were harvested and fixed in 4% paraformaldehyde overnight at 4 °C, washed and incubated in CUBIC reagent 1 (25% (w/w) urea, 25% (w/w) N,N,N',N'-tetrakis(2-hydroxypropyl)ethylenediamine, 15% (w/w) Triton X-100 in distilled water) for 4 days shaking at RT. After washing, the tissue was blocked using blocking buffer (5% FBS, 2% BSA, 1% Triton X-100, 0.02% sodium azide in PBS) overnight at RT, incubated with primary antibodies (Supplementary Table 2) diluted in blocking buffer for 3 days at 4 °C with rocking, washed three times for 2 h (0.05% Tween-20 in PBS) and incubated with DAPI (1 μg/ml) in blocking buffer. For cell proliferation

visualization in EdU-injected mice, the staining was performed using Click-iT imaging kit (Thermo Fisher Scientific) following the manufacturer's instructions. Then the glands were transferred to CUBIC reagent 2 (50% (w/w) sucrose, 25% (w/w) urea, 10% (w/w) 2,2′,2″-nitrilotriethanol, 0.1% (w/w) Triton X-100 in distilled water) for >1 day at RT with rocking. The samples were mounted with CUBIC reagent 2 between two coverslips with double-sided tape as a spacer to enable imaging from both sides; they were imaged on laser scanning confocal microscopes LSM780 or LSM880 (Zeiss). Non-fibroblastic cells were identified based on their morphology, position in the tissue and difference in GFP expression levels. Namely, the *Acta2-CreERT2* model induced GFP expression in basal epithelial cells, vascular smooth muscle cells and pericytes; the *Notch1-CreERT2* model induced GFP expression in a subset of luminal epithelial cells and in the endothelium; the *Fgf10-CreERT2* model induced GFP only in fibroblastic cells, with GFP+ cells with clear adipocyte morphology appearing after longer chase. The numbers of GFP+ cells were manually counted in the z-stack images. For quantification of position of GFP+ cells in the *Fgf10-CreERT2* model, epithelial TEBs were manually split into "head" (round, convex part), "neck" (the concave part connecting head and duct) and "subtending duct" (the part where diameter is not changing anymore) and the GFP+ cells within 50 µm from epithelium were counted.

Whole-mount mammary gland visualization with carmine

For visualization of mammary epithelial network with carmine, the mammary glands #4 were dissected, spread on a glass slide and fixed overnight in Carnoy's fixative (60% ethanol, 30% chloroform, 10% glacial acetic acid). Then the glands were rehydrated with series of ethanol (70%, 50%, distilled water) and stained overnight in carmine staining solution (0.1% (w/w) carmine, 0.25% (w/w) aluminium potassium sulphate in water). Then the glands were rinsed in water and dehydrated via a series of ethanol baths (50%, 70%, 90%, 100%) and finally cleared in xylene overnight, before imaging in xylene in closed glass container on a stereoscope.

Mammary fragment transplantation

For transplantation experiments, mammary gland #4 from 5-week old *R26-mTmG* females was harvested, spread on a 10 cm plastic petri dish and a $0.5 \times 0.5 \times 0.5$ mm³ piece containing epithelial duct was dissected under a stereoscope using tdTomato fluorescence for guidance (Leica FM165C) and kept in CO_2 independent medium on ice until use, but for maximum of 6 h. Three weeks old nude females were anesthetized with isoflurane, after disinfection of abdominal area, reversed Y-shaped incision was made into skin and #4 mammary glands were mobilized from the peritoneum. After cauterization of blood vessels in the connection of #5 and #4 mammary glands, the proximal part of #4 mammary gland (from the nipple to the lymph node) was cut out. Small incision using iris scissors was made in the middle of the remaining fat pad to create a capsule, where a single piece of *R26-mTmG* tissue was grafted. The skin opening was closed using biodegradable suture and mice were carefully monitored until full recovery. During first 2 weeks after surgery, mice were supplied with analgesia (0.2 mg/ml of Ibuprofen in drinking water). 3.5 weeks after the surgery, the mice were euthanized, and the mammary outgrowth was analysed.

Mammary organoid-fibroblast co-cultures

The 3D culture of mammary organoids and fibroblasts has been described in detail in a published protocol[75]. Briefly, for isolation of primary mammary organoids (fragments), mammary glands were harvested, finely chopped and enzymatically digested [2 mg/ml collagenase A, 2 mg/ml trypsin, 5 µg/ml insulin, 50 µg/ml gentamicin (all Merck), 5% FBS (Hyclone/GE Healthcare) in DMEM/F12 (Thermo Fisher Scientific)] for 30 min at 37 °C and 120 rpm. Resulting tissue suspension was treated with DNase I (20 U/ml; Merck) and enriched for

organoids by 5 rounds of differential centrifugation at $450 \times g$ for 10 s. The collagen/Matrigel gel matrix [MEM 1×, collagen 1 from rat tail (Corning) 2.5 mg/ml, 30% growth factor-reduced Matrigel (Corning)] was mixed and pre-incubated for 1 h on ice before mixing with cells. 100 organoids, 80,000 FACS-sorted fibroblasts and 25 µl of collagen/Matrigel gel matrix were mixed well and plated on small patches of Matrigel on 8-well coverslip-bottom dishes (IBIDI) and overlaid with basal organoid medium (1× ITS, 100 U/ml of penicillin, and 100 µg/ml of streptomycin in DMEM/F12).

Co-culture immunofluorescence

For immunofluorescence analysis of 3D co-cultures, cells were fixed with 4% paraformaldehyde for 40 min at RT, washed, and stored in PBS. The co-cultures were permeabilized with 0.5% Triton X-100 in PBS, blocked with 1% BSA, 5% FBS and 0.1% Triton X-100 in PBS (3D staining buffer, 3SB) and incubated with primary antibodies (Supplementary Table 2) in 3SB over 1–3 nights at 4 °C. Then the co-cultures were washed for 3 h with 0.05% Tween-20 in PBS and incubated with fluorophore-conjugated secondary antibodies (Thermo Fisher Scientific) and DAPI (1 µg/ml; Merck) in 3SB overnight at 4 °C in dark. Then the co-cultures were washed for 3 h with 0.05% Tween-20 in PBS, cleared with 60% glycerol overnight at RT in dark. The co-cultures were imaged using LSM 880 (Zeiss).

Statistics and reproducibility

The sample size of at least $n = 3$ for both in vivo and in vitro experiments was chosen in accord with standard practice in the field. No statistical method was used to predetermine sample size. No data were excluded from the analyses, the experiments were not randomized and the investigators were not blinded to allocation during experiments and outcome assessment. Statistical analysis was carried out in R using *stat_compare_means* function or *geom_signif* function of ggplot2 package. For comparing percentage, the *chisq.test* was used. *N* denotes number of samples used for statistical analysis, *n* denotes number of independent biological replicates, n.s. means not significant, $*p < 0.05$, $**p < 0.01$, $***p < 0.001$, $****p < 0.0001$. The exact *p*-values of statistical tests are provided in the Source data file. The bar plots show mean ± SD. The box plots show median, the box borders are Q2–Q3, the whiskers are minimum to maximum, big points are predicted outliers, dots show single samples.

Reporting summary

Further information on research design is available in the Nature Portfolio Reporting Summary linked to this article.

Data availability

The sequencing data generated in this study have been deposited in the ArrayExpress database under accession code E-MTAB-15262 (FACS-sorted stromal fraction) and E-MTAB-15259 (unsorted cells for Cell Chat analysis). Source data are provided with this paper.

References

1. Plikus, M. V. et al. Fibroblasts: origins, definitions, and functions in health and disease. *Cell* **184**, 3852–3872 (2021).
2. Sumbal, J., Belisova, D. & Koledova, Z. Fibroblasts: the grey eminence of mammary gland development. *Semin. Cell Dev. Biol.* **114**, 134–142 (2021).
3. Tomasek, J. J., Gabbiani, G., Hinz, B., Chaponnier, C. & Brown, R. A. Myofibroblasts and mechano-regulation of connective tissue remodelling. *Nat. Rev. Mol. Cell Biol.* **3**, 349–363 (2002).
4. Buechler, M. B. et al. Cross-tissue organization of the fibroblast lineage. *Nature* **593**, 575–579 (2021).
5. Muhl, L. et al. Single-cell analysis uncovers fibroblast heterogeneity and criteria for fibroblast and mural cell identification and discrimination. *Nat. Commun.* **11**, 3953 (2020).

6. Macias, H. & Hinck, L. Mammary gland development. *Wiley Interdiscip. Rev. Dev. Biol.* **1**, 533–557 (2012).

7. Paine, I. S. et al. A geometrically-constrained mathematical model of mammary gland ductal elongation reveals novel cellular dynamics within the terminal end bud. *PLoS Comput. Biol.* **12**, e1004839 (2016).

8. Hannezo, E. et al. A unifying theory of branching morphogenesis. *Cell* **171**, 242–255.e27 (2017).

9. Scheele, C. L. G. J. et al. Identity and dynamics of mammary stem cells during branching morphogenesis. *Nature* **542**, 313–331 (2017).

10. Wiseman, B. S. & Werb, Z. Stromal effects on mammary gland development and breast cancer. *Science* **296**, 1046–1049 (2002).

11. Zhang, X. et al. FGF ligands of the postnatal mammary stroma regulate distinct aspects of epithelial morphogenesis. *Development* **141**, 3352–3362 (2014).

12. Ewald, A. J., Brenot, A., Duong, M., Chan, B. S. & Werb, Z. Collective epithelial migration and cell rearrangements drive mammary branching morphogenesis. *Cell* **14**, 570–581 (2008).

13. Peuhu, E. et al. SHARPIN regulates collagen architecture and ductal outgrowth in the developing mouse mammary gland. *EMBO J.* **36**, 165–182 (2017).

14. Nguyen-Ngoc, K.-V. & Ewald, A. J. Mammary ductal elongation and myoepithelial migration are regulated by the composition of the extracellular matrix. *J. Microsc.* **251**, 212–223 (2013).

15. Brownfield, D. G. et al. Patterned collagen fibers orient branching mammary epithelium through distinct signaling modules. *Curr. Biol.* **23**, 703–709 (2013).

16. Nerger, B. A. et al. Local accumulation of extracellular matrix regulates global morphogenetic patterning in the developing mammary gland. *Curr. Biol.* **31**, 1903–1917.e6 (2021).

17. Sumbal, J., Fre, S. & Sumbalova Koledova, Z. Fibroblast-induced mammary epithelial branching depends on fibroblast contractility. *PLoS Biol.* **22**, e3002093 (2024).

18. Goodwin, K. et al. Smooth muscle differentiation shapes domain branches during mouse lung development. *Development* **146**, dev181172 (2019).

19. Heitman, N. et al. Dermal sheath contraction powers stem cell niche relocation during hair cycle regression. *Science* **367**, 161–166 (2020).

20. Schuster, R., Younesi, F., Ezzo, M. & Hin, B. The role of myofibroblasts in physiological and pathological tissue repair. *Cold Spring Harb. Perspect. Biol.* **15**, a041231 (2023).

21. Sahai, E. et al. A framework for advancing our understanding of cancer-associated fibroblasts. *Nat. Rev. Cancer* **20**, 174–186 (2020).

22. Barbazán, J. & Vignjevic, D. M. Cancer associated fibroblasts: is the force the path to the dark side?. *Curr. Opin. Cell Biol.* **56**, 71–79 (2019).

23. Houthuijzen, J. M. et al. CD26-negative and CD26-positive tissue-resident fibroblasts contribute to functionally distinct CAF subpopulations in breast cancer. *Nat. Commun.* **14**, 183 (2023).

24. Kanaya, N. et al. Single-cell RNA-sequencing analysis of estrogen- and endocrine-disrupting chemical-induced reorganization of mouse mammary gland. *Commun. Biol.* **2**, 406 (2019).

25. Li, C. M.-C. et al. Aging-associated alterations in mammary epithelia and stroma revealed by single-cell RNA sequencing. *Cell Rep.* **33**, 108566 (2020).

26. Yoshitake, R. et al. Single-cell transcriptomics identifies heterogeneity of mouse mammary gland fibroblasts with distinct functions, estrogen responses, differentiation processes, and crosstalks with epithelium. *Front. Cell Dev. Biol.* **10**, 850568 (2022).

27. Li, J. et al. Sprouty genes regulate activated fibroblasts in mammary epithelial development and breast cancer. *Cell Death Dis.* **15**, 1–15 (2024).

28. Pascual, R. et al. Fibroblast hierarchy dynamics during mammary gland morphogenesis and tumorigenesis. *EMBO J.* https://doi.org/10.1038/s44318-025-00422-3 (2025).

29. Paine, I. S. & Lewis, M. T. The terminal end bud: the little engine that could. *J. Mammary Gland Biol. Neoplasia* **22**, 93–108 (2017).

30. Bartoschek, M. et al. Spatially and functionally distinct subclasses of breast cancer-associated fibroblasts revealed by single cell RNA sequencing. *Nat. Commun.* **9**, 5150 (2018).

31. Stingl, J. et al. Purification and unique properties of mammary epithelial stem cells. *Nature* **439**, 993–997 (2006).

32. Merrick, D. et al. Identification of a mesenchymal progenitor cell hierarchy in adipose tissue. *Science* **364**, eaav2501 (2019).

33. Chen, M. et al. Identification of an adipose tissue-resident pro-preadipocyte population. *Cell Rep.* **42**, 112440 (2023).

34. Carabaña, C. et al. Spatially distinct epithelial and mesenchymal cell subsets along progressive lineage restriction in the branching embryonic mammary gland. *EMBO J.* **43**, 2308–2336 (2024).

35. Feinberg, T. Y. et al. Divergent matrix-remodeling strategies distinguish developmental from neoplastic mammary epithelial cell invasion programs. *Dev. Cell* **47**, 145–160.e6 (2018).

36. Jin, S. et al. Inference and analysis of cell-cell communication using CellChat. *Nat. Commun.* **12**, 1088 (2021).

37. Pal, B. et al. Single cell transcriptome atlas of mouse mammary epithelial cells across development. *Breast Cancer Res.* **23**, 69 (2021).

38. Schwalie, P. C. et al. A stromal cell population that inhibits adipogenesis in mammalian fat depots. *Nature* **559**, 103–108 (2018).

39. Dong, H. et al. Identification of a regulatory pathway inhibiting adipogenesis via RSPO2. *Nat. Metab.* **4**, 90–105 (2022).

40. Fre, S. et al. Notch lineages and activity in intestinal stem cells determined by a new set of knock-in mice. *PLoS ONE* **6**, e25785 (2011).

41. Wendling, O., Bornert, J.-M., Chambon, P. & Metzger, D. Efficient temporally-controlled targeted mutagenesis in smooth muscle cells of the adult mouse. *Genesis* **47**, 14–18 (2009).

42. Lloyd-Lewis, B. et al. Imaging the mammary gland and mammary tumours in 3D: optical tissue clearing and immunofluorescence methods. *Breast Cancer Res.* **18**, 127 (2016).

43. Susaki, E. A. et al. Whole-brain imaging with single-cell resolution using chemical cocktails and computational analysis. *Cell* **157**, 726–739 (2014).

44. Stefkovich, M., Traynor, S., Cheng, L., Merrick, D. & Seale, P. Dpp4+ interstitial progenitor cells contribute to basal and high fat diet-induced adipogenesis. *Mol. Metab.* **54**, 101357 (2021).

45. Chu, X. et al. Validation of a novel Fgf10 Cre-ERT2 knock-in mouse line targeting FGF10Pos cells postnatally. *Front. Cell Dev. Biol.* **9**, 671841 (2021).

46. Driskell, R. R. et al. Distinct fibroblast lineages determine dermal architecture in skin development and repair. *Nature* **504**, 277–281 (2013).

47. Cordero-Espinoza, L. et al. Dynamic cell contacts between periportal mesenchyme and ductal epithelium act as a rheostat for liver cell proliferation. *Cell Stem Cell* **28**, 1907–1921.e8 (2021).

48. Lepreux, S. & Desmoulière, A. Human liver myofibroblasts during development and diseases with a focus on portal (myo)fibroblasts. *Front. Physiol.* **6**, 173 (2015).

49. Driskell, R. R., Jahoda, C. A. B., Chuong, C.-M., Watt, F. M. & Horsley, V. Defining dermal adipose tissue. *Exp. Dermatol.* **23**, 629–631 (2014).

50. Goss, G., Rognoni, E., Salameti, V. & Watt, F. M. Distinct fibroblast lineages give rise to NG2+ pericyte populations in mouse skin development and repair. *Front. Cell Dev. Biol.* **9**, 675080 (2021).

51. Sun, C., Berry, W. L. & Olson, L. E. PDGFRα controls the balance of stromal and adipogenic cells during adipose tissue organogenesis. *Development* **144**, 83–94 (2017).

52. Wang, Q. A. et al. Reversible De-differentiation of mature white adipocytes into preadipocyte-like precursors during lactation. *Cell Metab.* **28**, 282–288.e3 (2018).

53. Zwick, R. K. et al. Adipocyte hypertrophy and lipid dynamics underlie mammary gland remodeling after lactation. *Nat. Commun.* **9**, 3592 (2018).

54. Sumbal, J., Vranova, T. & Koledova, Z. FGF signaling dynamics regulates epithelial patterning and morphogenesis. Preprint at https://doi.org/10.1101/2020.11.17.386607 (2020).

55. Fata, J. E., Werb, Z. & Bissell, M. J. Regulation of mammary gland branching morphogenesis by the extracellular matrix and its remodeling enzymes. *Breast Cancer Res.* **6**, 1–11 (2004).

56. Paramore, S. V., Goodwin, K. & Nelson, C. M. How to build an epithelial tree. *Phys. Biol.* **19**, 061002 (2022).

57. Schedin, P. & Keely, P. J. Mammary gland ECM remodeling, stiffness, and mechanosignaling in normal development and tumor progression. *Cold Spring Harb. Perspect. Biol.* **3**, a003228 (2011).

58. Li, R., Li, X., Hagood, J., Zhu, M.-S. & Sun, X. Myofibroblast contraction is essential for generating and regenerating the gas-exchange surface. *J. Clin. Invest.* **130**, 2859–2871 (2020).

59. Shyer, A. E. et al. Emergent cellular self-organization and mechanosensation initiate follicle pattern in the avian skin. *Science* **357**, 811–815 (2017).

60. Villeneuve, C. et al. Mechanical forces across compartments coordinate cell shape and fate transitions to generate tissue architecture. *Nat. Cell Biol.* **26**, 207–218 (2024).

61. Shyer, A. E. et al. Villification: how the gut gets its villi. *Science* **342**, 212–218 (2013).

62. Neumann, N. M. et al. Coordination of receptor tyrosine kinase signaling and interfacial tension dynamics drive radial intercalation and tube elongation. *Dev. Cell* **45**, 67–82.e6 (2018).

63. Hammer, A. M. et al. Stromal PDGFR-α activation enhances matrix stiffness, impedes mammary ductal development, and accelerates tumor growth. *Neoplasia* **19**, 496–508 (2017).

64. Sumbal, J. & Koledova, Z. FGF signaling in mammary gland fibroblasts regulates multiple fibroblast functions and mammary epithelial morphogenesis. *Development* **146**, dev185306 (2019).

65. Rajaram, R. D. et al. Progesterone and Wnt4 control mammary stem cells via myoepithelial crosstalk. *EMBO J.* **34**, 641–652 (2015).

66. van Amerongen, R., Bowman, A. N. & Nusse, R. Developmental stage and time dictate the fate of Wnt/β-catenin-responsive stem cells in the mammary gland. *Cell Stem Cell* **11**, 387–400 (2012).

67. Wang, J. et al. Endothelial Wnts control mammary epithelial patterning via fibroblast signaling. *Cell Rep.* **34**, 108897 (2021).

68. Lodyga, M. et al. Cadherin-11–mediated adhesion of macrophages to myofibroblasts establishes a profibrotic niche of active TGF-β. *Sci. Signal.* **12**, eaao3469 (2019).

69. Gouon-Evans, V., Rothenberg, M. E. & Pollard, J. W. Postnatal mammary gland development requires macrophages and eosinophils. *Development* **127**, 2269–2282 (2000).

70. Gyorki, D. E., Asselin-Labat, M.-L., van Rooijen, N., Lindeman, G. J. & Visvader, J. E. Resident macrophages influence stem cell activity in the mammary gland. *Breast Cancer Res.* **11**, R62 (2009).

71. Riedl, J. et al. Lifeact mice for studying F-actin dynamics. *Nat. Methods* **7**, 168–169 (2010).

72. Muzumdar, M. D., Tasic, B., Miyamichi, K., Li, L. & Luo, L. A global double-fluorescent Cre reporter mouse. *Genesis* **45**, 593–605 (2007).

73. Zheng, B., Zhang, Z., Black, C. M., de Crombrugghe, B. & Denton, C. P. Ligand-dependent genetic recombination in fibroblasts: a potentially powerful technique for investigating gene function in fibrosis. *Am. J. Pathol.* **160**, 1609–1617 (2002).

74. Hao, Y. et al. Integrated analysis of multimodal single-cell data. *Cell* **184**, 3573–3587.e29 (2021).

75. Koledova, Z. & Lu, P. A 3D fibroblast-epithelium co-culture model for understanding microenvironmental role in branching morphogenesis of the mammary gland. *Methods Mol. Biol.* **1501**, 217–231 (2017).

Author contributions

J.S. conceptualized the work, performed the experiments, analyzed data and wrote the original manuscript. Z.S.K. and S.F. acquired funding, conceptualized and supervised the work and wrote the manuscript. R.J. performed the CellChat analysis of scRNAseq data. K.A. performed clearing and imaging of mammary glands for *Fgf10* lineage tracing. C.M. performed the single cell sequencing. M.M.F. contributed to experimental work and edited the manuscript. V.D. performed histological analysis of mammary glands for *Fgf10* lineage tracing.

Competing interests

The authors declare no conflict of interest.

Additional information

Supplementary information The online version contains supplementary material available at https://doi.org/10.1038/s41467-025-63612-x.

Correspondence and requests for materials should be addressed to Zuzana Sumbalova Koledova or Silvia Fre.

Peer review information *Nature Communications* thanks the anonymous reviewers for their contribution to the peer review of this work. A peer review file is available.

Reprints and permissions information is available at http://www.nature.com/reprints

Publisher's note Springer Nature remains neutral with regard to jurisdictional claims in published maps and institutional affiliations.